Journal of Geophysical Research: Earth Surface

RESEARCH ARTICLE
10.1029/2018JF004768

Numerical Modeling of Iceberg Capsizing Responsible for Glacial Earthquakes

Amandine Sergeant[1,2,3], Vladislav A. Yastrebov[4], Anne Mangeney[1,2,5], Olivier Castelnau[6], Jean-Paul Montagner[1,2], and Eléonore Stutzmann[1]

[1]Institut de Physique du Globe de Paris, CNRS UMR 7154, Université Paris Diderot-Paris 7, Paris, France, [2]Université Paris Diderot, Paris, France, [3]Now at Versuchsanstalt für Wasserbau, Hydrologie und Glaziologie (VAW), ETH Zürich, Zürich, Switzerland, [4]MINES ParisTech, PSL Research University, Centre des Matériaux, CNRS UMR 7633, Evry, France, [5]ANGE team, INRIA, Laboratoire Jacques-Louis Lions, Paris, France, [6]Processes and Engineering in Mechanics and Materials, CNRS UMR 8006, ENSAM, CNAM, Paris, France

Key Points:
- We present a numerical mechanical model of iceberg capsize which allows to compute the iceberg-to-terminus contact force responsible for glacial earthquake generation
- The force amplitude of glacial earthquake magnitude does not linearly scale with the iceberg volume due to hydrodynamic effects
- The force history and spectral energy distribution varies with the initial buoyancy state of the iceberg, calving style, and iceberg geometry

Supporting Information:
- Supporting Information S1
- Movie S1
- Movie S2
- Movie S3
- Figure S1
- Figure S2

Correspondence to:
A. Sergeant,
sergeant@vaw.baug.ethz.ch

Citation:
Sergeant, A., Yastrebov, V. A., Mangeney, A., Castelnau, O., Montagner, J.-P., & Stutzmann, E. (2018). Numerical modeling of iceberg capsizing responsible for glacial earthquakes. *Journal of Geophysical Research: Earth Surface*, *123*, 3013–3033. https://doi.org/10.1029/2018JF004768

Received 22 MAY 2018
Accepted 24 OCT 2018
Accepted article online 29 OCT 2018
Published online 22 NOV 2018

Abstract The capsizing of icebergs calved from marine-terminating glaciers generate horizontal forces on the glacier front, producing long-period seismic signals referred to as *glacial earthquakes*. These forces can be estimated by broadband seismic inversion, but their interpretation in terms of magnitude and waveform variability is not straightforward. We present a numerical model for fluid drag that can be used to study buoyancy-driven iceberg capsize dynamics and the generated contact forces on a calving face using the finite-element approach. We investigate the sensitivity of the force to drag effects, iceberg geometry, calving style, and initial buoyancy. We show that there is no simple relationship between force amplitude and iceberg volume, and similar force magnitudes can be reached for different iceberg sizes. The force history and spectral content varies with the iceberg attributes. The iceberg aspect ratio primarily controls the capsize dynamics, the force shape, and force frequency, whereas the iceberg height has a stronger impact on the force magnitude. Iceberg hydrostatic imbalance generates contact forces with specific frequency peaks that explain the variability in glacial earthquake dominant frequency. For similar icebergs, top-out and bottom-out events have significantly different capsize dynamics leading to larger top-out forces especially for thin icebergs. For realistic iceberg dimensions, we find contact-force magnitudes that range between 5.6×10^{11} and 2×10^{14} kg·m, consistent with seismic observations. This study provides a useful framework for interpreting glacial earthquake sources and estimating the ice mass loss from coupled analysis of seismic signals and modeling results.

Plain Language Summary Glacial earthquakes originate from fast-moving outlet glaciers in Greenland. They are produced by kilometer-scale iceberg calving and capsizes, have equivalent magnitudes of 5, and are recorded at several thousands of kilometers from Greenland. These earthquakes were discovered in 2003 and have significantly contributed to the study of seismic signals generated in glaciers to investigate the impact of climate changes on the glacier dynamics. The interpretation of their source characteristic is still not possible as the understanding of the source processes is limited. We develop here a numerical mechanical modeling of iceberg capsize (turn in water against the glacier terminus) to investigate the force responsible for such events. We analyze the variations of the force with iceberg geometry, initial state of buoyant equilibrium and calving style and we relate them to seismic observations. We find that the force amplitude does not simply scale with the iceberg volume. For individual capsize events, the force time evolution and its frequency content are primarily controlled by the iceberg individual dimensions, particularly its width, and the calving mode. This study provides first keys to interpret glacial earthquake sources and estimate the ice mass loss from the seismic signal when coupled to the modeling results.

1. Introduction

Rapid glacier thinning and increasing calving rates have been measured at marine-terminating glacial termini in Greenland since the 2000s (e.g., Joughin et al., 2004; Howat et al., 2007). This rise in the number of calving events is synchronous with an increase of particular cryoseismic events referred to as *glacial earthquakes* (e.g., Ekström et al., 2003; Nettles & Ekström, 2010; Olsen & Nettles, 2017; Veitch & Nettles, 2012). Iceberg calving

and, more generally, instabilities in the margins of tidewater glaciers generate a wide spectrum of seismic signals. Signal characteristics differ due to various source mechanisms (for a review, Podolskiy & Walter, 2016). In particular, for calving events, seismic emissions can be associated with ice fracturing (e.g., O'Neel et al., 2007; Walter et al., 2010), iceberg scraping or impacting on the calving front (Amundson et al., 2008; Tsai et al., 2008; Walter et al., 2012), ice avalanches (Sergeant et al., 2016), ice-mélange dynamics (Amundson et al., 2010; Sergeant et al., 2016), glacier deformation, lift and basal slip (Murray, Nettles, et al., 2015; Tsai et al., 2008), or a complex combination of these processes. All of them can occur simultaneously during a calving sequence and it is not easy to distinguish between the seismic signals generated by each source mechanism (Sergeant et al., 2016). The seismic source characteristics (amplitude, duration and evolution with time) are related to the dynamic processes that are involved. They should depend on rheological and dimensional parameters as has been shown for landslide events (Ekström & Stark, 2013; Favreau et al., 2010; Moretti et al., 2012; Moretti et al., 2015; Yamada, Mangeney, Matsushi & Moretti, 2018; Yamada, Mangeney, Matsushi & Matsuzawai, 2018; Zhao et al., 2014). Detailed comparison of the force history inverted from seismic data with the force calculated by landslide models provides a unique way to determine the characteristics and dynamics of natural landslides. Glacial earthquake interpretation and characterization in terms of source mechanisms and ice mass loss are therefore limited since dynamic processes are difficult to quantify and discriminate between each other.

Glacial earthquakes produce long-period waves (10–150 s) that propagate over teleseismic distances (i.e., ≥1,000 km). Generated seismic waves are best modeled with a near-horizontal source-force acting and pointing upglacier, normal to the calving front (e.g., Olsen & Nettles, 2017; Veitch & Nettles, 2012; Walter et al., 2012). Using a mechanical model, Tsai et al. (2008) first showed that among all possible cryogenic sources, only basal slip and iceberg capsizing (ice-block rotation in water with contact against the glacier terminus) were able to produce high magnitude and long-period cryoseismic signals. They further showed that the contact force produced by a tipping iceberg on the calving front is the prevailing source for glacial earthquakes. However, to determine the observed range of force amplitudes and durations derived from seismic data inversions, they needed to modify the rotating iceberg inertia due to the presence of ice-mélange in the proglacial fjord.

Sergeant et al. (2016) inverted the force for a calving episode captured at the Jakobshavn Isbrae, using the broadband seismic signals at frequencies of dominant energy 0.01–0.1 Hz. In particular, they found similar durations (∼150 s) and amplitudes ($\sim 1 \times 10^{10}$ N) for the forces associated with the bottom-out (BO) and top-out (TO) capsize of two icebergs of different sizes. However, the difference between the forces generated by BO (i.e., the iceberg bottom drifts away from the terminus while rotating) and TO (i.e., the iceberg top drifts away from the terminus) capsizes is not reproduced by the model proposed by Tsai et al. (2008), even though such a difference is also observed in laboratory experiments of iceberg capsizes (Amundson, Burton, et al., 2012). Field and laboratory observations reveal that glacial earthquake magnitude appears to depend not only on the iceberg volume but also on the capsize dynamics related to the calving style. Tsai et al. (2008) and Walter et al. (2012) showed that the synthetic long-period seismic waveforms are insensitive to the choice of the force time-function, notably due to filtering effects. Nevertheless, the force inverted by Sergeant et al. (2016) shows a complex history that varies from one event to another and cannot be described exactly by simple force-source models that have a limited number of parameters. To interpret the complexity and variability of the time-evolution of the force inverted from seismic data, a precise mechanical model for iceberg capsize is needed.

Tsai et al. (2008) and then Amundson, Burton, et al. (2012) first derived models for the contact force between a box-shaped rigid block capsizing in water against a vertical wall. Tsai et al. (2008) used an added mass to model the additional inertia of the iceberg due to the water-mass displacement during its motion and neglected energy dissipation due to water drag and viscous effects. Amundson, Burton, et al. (2012) accounted for the contribution of water drag to the capsize dynamics. They tested several drag force laws to compute iceberg capsize motion and generated contact forces, which were then fitted to centimeter-scale laboratory measurements conducted at intermediate Reynolds number $Re \approx 10^4$. Their analysis reveals that accounting for water drag is crucial for reproducing the observations and that most of the potential-energy excess of the capsizing iceberg is dissipated. Both modeling approaches (Tsai et al., 2008; Amundson, Burton, et al., 2012) show that the contact-force history depends on the iceberg dimensions, on the hydrodynamic forces (including hydrostatic pressure and depending on the model: added mass or drag forces) and also on the capsize dynamics. Therefore, even for these oversimplified models of iceberg/water/wall interaction, the analytical expression of the force can hardly be derived in a closed form.

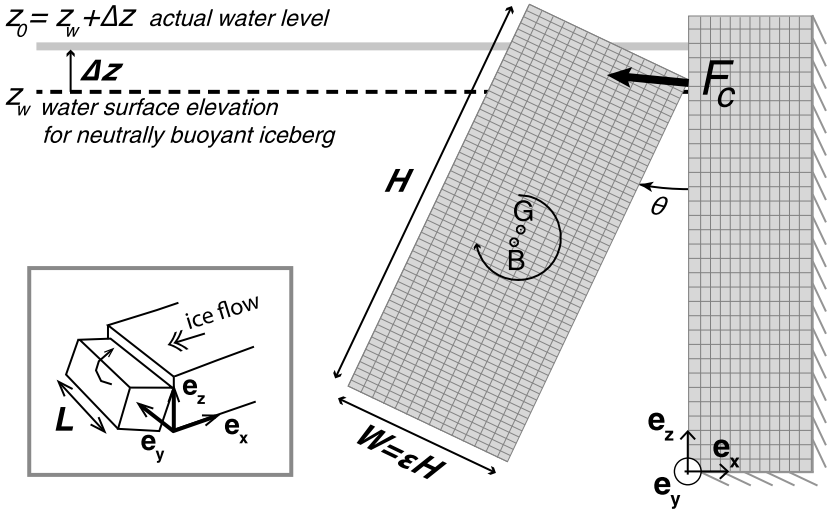

Figure 1. Geometry and parameters of the system: iceberg aspect ratio ϵ, height H, and perturbation of the water level Δz for initial hydrostatic equilibrium of the ice block. The iceberg across-glacier length L is in the y-direction. G and B are the center of mass of the iceberg and of its submerged part, respectively. The ice wall is fixed vertically and horizontally. The contact force F_c is integrated over the vertical rear face of the wall.

Here we propose an alternative model for capsizing iceberg which accounts for hydrostatic pressure and approximately for dynamic fluid-structure interactions (pressure drag). This model is integrated in a finite-element framework and therefore is compatible with elastic deformation of floating (and interacting) solids. The used drag model is more accurate than what was used in Amundson, Burton, et al. (2012) and is thus able to capture an important difference between top-out and bottom-out capsize; however, the added mass is not taken into account in our model. A detailed comparison of our model with the existing ones is provided in section 2.2.3.

Following the work of Tsai et al. (2008), Amundson, Burton, et al. (2012), and Burton et al. (2012), the aim of this study is to more deeply explore the dynamic processes involved in glacial earthquakes and their influence on the generated forces. We investigate in detail the capsizing-force variation in terms of amplitude, duration, shape, and spectral content with iceberg dimensions and the initial configuration. We compile catalogs of simulated force histories to guide the interpretation of forces inverted from glacial earthquakes.

The paper is organized as follows. We first present our model of fluid-structure interaction and compare it with existing models (section 2). In sections 3 and 4, we analyze the results for the force generated by BO and TO capsizing of icebergs of variable dimensions and compare them to other available observations (laboratory experiments and seismic inversions). Finally, in section 5, we show the influence of the initial buoyant conditions of the icebergs on the generated forces. Our conclusions emphasize the potential of our approach for the quantification of iceberg characteristics from seismic signals.

2. Iceberg-Capsize Model

We study the interaction between a box-shaped iceberg capsizing in the sea and an immobile vertical wall, which represents the postcalving front of the glacier (Figure 1). In nature, the height of capsizing icebergs that produce glacial earthquakes is observed to be the full glacier thickness as this kind of calving occurs when the glacier terminus is near grounded (Amundson et al., 2008; Amundson et al., 2010). The iceberg width is determined by the crevasse network and may vary over a large distance of up to tens of km. To capsize spontaneously, icebergs should have a relatively small aspect ratio (width/height < 0.75). Since their motion is constrained by the glacier terminus, these unstable icebergs drift outward and rise up while rotating. Icebergs of greater aspect ratios are buoyantly stable and will not capsize without additional perturbations (Burton et al., 2012).

The iceberg drift and rotational motion implies a contact interaction between the iceberg and the glacier terminus. The evolution of the contact force, which is transmitted to the solid Earth, is controlled by the iceberg's capsize dynamics, which is primarily determined by its interaction with sea water.

Table 1
List of Model Parameters Used in All Simulations

Parameter	Symbol	Value(s)
Iceberg height	H	500–1,050 m
Iceberg aspect ratio	ϵ	0.1–0.7
Iceberg length	L	500–5,000 m
Ice Young's modulus	E	9.3 GPa
Ice Poisson coefficient	ν	0.3
Ice-ice friction	μ	0
Ice density	ρ_i	917 kg/m^3
Sea water density	ρ_w	1,025 kg/m^3

The process of iceberg's capsize and the associated behavior of the glacier being complex, several simplifications are made in our model. The main assumption is the simplified fluid-structure interaction, which does not resolve costly Navier-Stokes equations including free surface, friction and contact between deformable solids. It is assumed that the fluid exerts on the iceberg a depth-dependent hydrostatic pressure and resists to iceberg's motion via the pressure drag, whose detailed description is given below. Real glaciers obey an elasto-viscoplastic mechanical behavior (e.g., Castelnau et al., 2008; Montagnat et al., 2014; Vaughan, 1995). Here, for the sake of simplicity, the deformation of the glacier is not taken into account similarly to existing models(Amundson, Burton, et al., 2012; Tsai et al., 2008). Crack initiation and propagation between the iceberg-to-be-calved and the terminus (e.g., Krug & Durand, 2014) is also neglected in our model since it can be considered that this process involves only high-frequency ($\geq$1 Hz) energy (e.g., Amundson et al., 2010; Tsai et al., 2008) and thus is of no interest for the low-frequency band in which glacial earthquakes are studied. The iceberg is thus assumed to be initially detached and tilted by a small angle. Finally, during the interaction of the calved iceberg with the terminus, ice fracturing and avalanches are also observed (Amundson et al., 2010; Sergeant et al., 2016), which are associated with energy dissipation and therefore can affect the overall system dynamics. These details were not taken into account neither. In addition, a recent work suggested that iceberg capsizing may induce a low-pressure zone beneath the floating tongue of the glacier (Murray, Nettles, et al., 2015). These authors argue that the resulting downward bending of the ungrounded terminus may be responsible for at least a part of the vertical component of the glacial earthquake force. This effect is not considered in our model and will be dealt with in future work.

2.1. Problem Setup

We investigate the capsize of an iceberg with a rectangular section of height H and width W. We define the iceberg aspect ratio as $\epsilon = W/H$ (Figure 1). The iceberg's motion is restricted by an immobile vertical wall representing the glacier's terminus. We use a coordinate system in which the axis $\vec{e}_z$ is vertical upwards, and $\vec{e}_x$ is horizontal pointing towards the glacier terminus. We denote by ρ_i the ice density (numerical values are listed in Table 1), $m = \rho_i HW$ is the iceberg mass, and G denotes its center of mass. Iceberg rotation is expressed by the angle θ measured clockwise from the vertical.

The iceberg is partly submerged in water (density ρ_w). The water surface elevation controls the hydrostatic equilibrium of the iceberg at the capsize initiation. We denote by z_w the water level corresponding to neutral buoyancy (i.e., iceberg at vertical equilibrium if $\theta = 0$). Neutral buoyancy at small initial angle θ_0 is obtained for $z_w - z_G = H\cos\theta_0\left(\frac{\rho_i}{\rho_w} - \frac{1}{2}\right)$ when the top of the iceberg surface lies entirely above sea level (z_G gives the vertical position of the center of mass G). As the glacier terminus is not necessarily neutrally buoyant at the moment of iceberg's release, we also investigate how the initial water level affects the capsize dynamics and the generated force. We call z_0 the actual water level and $\Delta z = z_0 - z_w$ the specified water level perturbation around the equilibrium level.

An initial small iceberg tilt θ_0 is specified. We used $\theta_0 = 1°$ for bottom-out (BO) events, and $\theta_0 = -1°$ for top-out (TO) events. The upper right or lower right corners are in contact with the terminus at time $t = 0$, respectively for BO and TO events. Note that the initial tilt angle affects the duration of the calving event, given that the iceberg initially moves very slowly away from its unstable equilibrium position $\theta = 0°$, but as long as the initial angle remains small, it does not affect the resulting contact force's evolution at later stages.

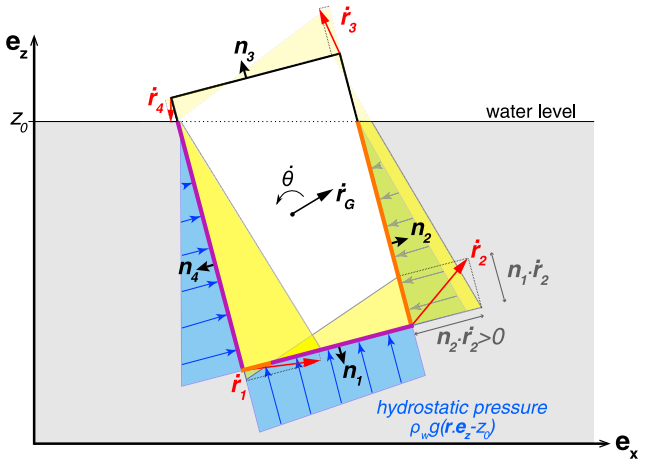

Figure 2. Illustration of a 2-D iceberg capsizing in water and pressures applied on the surface elements. Here is represented a box-shaped iceberg with surface elements equal to the side length, with local outward normal vector $\mathbf{n}(\mathbf{r})$. The static water pressure (inward blue arrows) applied to the iceberg boundary increases linearly with surface element depth. The yellow areas represent the profiles of normal velocities $v_n(\mathbf{r}) = \dot{\mathbf{r}} \cdot \mathbf{n}$ along each boundary segment. Submerged surface boundaries are plotted in purple when the pressure related to drag (equation (2)) is collinear to the local normal vector $\mathbf{n}$ (toward the outside of the iceberg) as the local normal component of the velocity is negative ($\dot{\mathbf{r}} \cdot \mathbf{n} < 0$). On the opposite, orange boundaries are when the pressure drag direction is toward the inside of the iceberg as $\dot{\mathbf{r}} \cdot \mathbf{n} > 0$.

For sake of simplicity we assume a purely elastic behavior of the ice. Like Petrenko and Whitworth (1999) and Montagnat et al. (2014), we used Young's modulus $E = 9.3$ GPa and Poisson ratio $\nu = 0.3$. although some field measurements suggest smaller values of E (Vaughan, 1995). The resulting elastic deformation occurring in the iceberg under the action of water and contact is negligible and does not affect its dynamics and the resulting contact force, that is, the motion of the deformable iceberg is indistinguishable from the rigid iceberg considered in Tsai et al. (2008).

Since we study a two-dimensional problem here, all forces F have units N/m and represent the linear force density in the y-direction (Figure 1). The real force acting on a 3-D box-shaped iceberg of a given length L along the calving front can be estimated as $F \times L$ when L is large compared to H.

2.2. Iceberg Dynamics

2.2.1. Formulation

The iceberg is subjected to the following forces, which are time dependent (except the constant ice weight): (i) The ice weight $\vec{F}_g = -\rho_i WHg\vec{e}_z$ (g is the gravitational acceleration). (ii) The upward buoyant force $\vec{F}_{hs}$ associated with the hydrostatic water pressure, which at depth $z_0 - z$ is given by $\rho_w g(z_0 - z)$, and thus

$$\vec{F}_{hs} = -\rho_w g \int_{\Gamma^{sub}} (z_0 - z)\vec{n}(\vec{r})\, d\Gamma, \tag{1}$$

where $\vec{n}(\vec{r})$ is the local outward normal vector of the iceberg surface at position $\vec{r}$ and Γ^{sub} is the contour of the submerged surface (Figure 2). (iii) The frictional contact force $\vec{F}_c = F_x\vec{e}_x + F_z\vec{e}_z$ acting at a corner of the iceberg. The sliding of the iceberg against the immobile wall is assumed to be governed by Coulomb's friction law. The vertical component of the contact force, F_z, is then equal to the horizontal force component F_x multiplied by the ice-ice dynamic friction coefficient μ: $|F_z(t)| = \mu|F_x(t)|$ when sliding occurs. Possible values for μ are discussed in Appendix B. (IV) The fluid drag force $\vec{F}_D$ resulting from the interaction between the moving iceberg and the surrounding water, which opposes iceberg's motion.

The drag force depends on the fluid density, viscosity, and flow regime and varies in response to the complex fluid motion around the object. Two types of drag forces can be distinguished: pressure and friction drag. Pressure drag ($\vec{F}_{D_p}$) is equal to the integral of the fluid overpressure along the solid (the term over-pressure is used here to highlight this pressure compared to the background hydrostatic pressure of water), and friction drag ($\vec{F}_{D_f}$) is the integral of shearing forces appearing due to local shearing of the fluid layer in tangential motion. To determine accurately these drag forces, a direct numerical simulation of iceberg rotation in water with a free surface, governed by the Navier-Stokes equation, would be needed. However, direct solution of these equations in presence of deformable solids and contact dynamics is highly challenging. To simplify the problem, we assume that the over-pressure at every elemental area of the iceberg's surface is given by

$$\vec{p}_d = -\frac{C}{2}\rho_w v_n^2 \text{sign}\,(v_n)\vec{n}, \tag{2}$$

where $\vec{v}$ is the iceberg velocity at the considered position $\vec{r}$, $v_n = \vec{v}\cdot\vec{n}$ is the normal component of this velocity, and C is a dimensionless scaling coefficient. We assume here $C \approx 1$ as suggested by the analysis of Munson et al. (2012). Note also that we assume that the relative fluid-solid velocity is determined solely by the solid velocity $\vec{v}$. The resulting pressure-drag force (linear density) is then computed as

$$\vec{F}_{D_p} = -\frac{\rho_w}{2}\int_{\Gamma^{sub}} v_n^2 \text{sign}\,(v_n)\vec{n}\, d\Gamma \tag{3}$$

The friction drag can be considered to be proportional to $Re^{-1/2}$ (Munson et al., 2012, pp. 489–502) where $Re = \rho_w VL/\mu_w$ is the Reynolds number with V being the average relative velocity of the calving iceberg with

respect to the fluid, L a characteristic dimension that can be taken to be one fourth of the iceberg perimeter, that is, $L = H(1+\epsilon)/2$, and μ_w the dynamic viscosity of the water. As it is discussed in Appendix A, for a kilometer-scale capsizing iceberg, the Reynolds number is of the order of 10^{11}. Consequently, the friction drag $\vec{F}_{D_f}$ can be reasonably neglected compared to the pressure drag. The former is thus not included in the general force balance. A more detailed justification of the choices made in our hydrodynamic model is presented in section 2.2.3 and Appendix A.

Neglecting the deformation of the iceberg leads to a simple system of equations for the coordinates $\vec{r}_G$ of the center of mass G and the inclination angle θ (Newton's second law):

$$\begin{cases} m\ddot{\vec{r}}_G = \vec{F}_g + \vec{F}_{hs} + \vec{F}_c + \vec{F}_{D_p} \\ I\ddot{\theta} = M_{hs} + M_c + M_D \end{cases} \tag{4}$$

where $m = \rho_i HW$ is the linear mass density, M_{hs}, M_c, and M_D are the moments of the corresponding forces F_{hs}, F_c, F_D calculated at the center of mass G, and $I = m(H^2 + W^2)/12$ is the moment of inertia computed at the center of mass. Note that we neglected the added water mass and added hydrodynamic moment of inertia (Wendel, 1956), which were partly taken into account in the model from Tsai et al. (2008).

2.2.2. Numerical Implementation

Since our long-term aim is to investigate the seismic signals generated by a large variety of capsizing icebergs for various glacier/iceberg/earth/sea configurations and to study possible destabilization of the upstream glacier flow (e.g., initiation of basal slip events), the proposed simplified fluid-structure interaction model was implemented within a finite-element framework. In the future, this implementation could be readily used for this general purpose, even though for the current study a simpler rigid model would be sufficient.

In order to include the interaction with water (equations 1 and 2), specific surface elements were implemented in Z-set finite-element software (Besson & Foerch, 1997). These elements incorporate the virtual work of the hydrostatic and drag fluid pressure into the global finite-element weak formulation. Integration of drag pressures over partly submerged elements (elements that are cut by the water surface) is done only on the submerged part, which ensures discretization-independent results. Thus, since we are not interested in resulting stress fields inside the ice, the results are practically independent of the mesh density. Using a relatively long time step of 1 s (i.e., comparable to the time needed for elastic waves to travel a distance similar to the iceberg dimension) smooths the resulting force by removing high-frequency oscillations coming from wave dynamics in the presence of contact. Thanks to this time smoothing, the resulting contact force and overall iceberg dynamics is directly comparable with the dynamics of rigid models (Amundson, Burton, et al., 2012; Tsai et al., 2008). The contact between the iceberg and the terminus wall is modeled using a node-to-segment approach within the direct method suggested in Francavilla and Zienkiewicz (1975) and Jean (1995). The Hilber-Hughes-Taylor method (Hilber et al., 1977) was used to integrate solid mechanics equations in time.

2.2.3. Comparison to Existing Capsize Models

To model iceberg capsize, Tsai et al. (2008) and Amundson, Burton, et al. (2012) solved the motion equations for a system similar to the one studied here (a rectangular iceberg against a vertical wall). As long the iceberg remains in contact with the wall, the authors calculated the horizontal and vertical positions of the iceberg center of mass, the inclination angle θ, and the horizontal contact force assuming a frictionless contact between the iceberg and the wall. The main difficulty is to model hydrodynamic effects without solving the complete set of Navier-Stokes equations for the fluid with a free surface and with a moving solid. These effects are described in different ways in Tsai et al. (2008) and Amundson, Burton, et al. (2012). We propose here a new formulation for the reasons explained below.

No drag was used in Tsai et al. (2008); however, the authors used added mass to account for the mass of displaced surrounding water (Brennen, 1982; Yvin et al., 2018). The added mass concept consists in adding to the iceberg the mass and moment of inertia of the surrounding water volume that is deflected during iceberg motion. In the motion equations (equation (4)), the resulting effective iceberg mass is then the sum of the ice mass M_g and the added mass corresponding to the mass of the displaced water, which varies with the direction of iceberg motion (and similarly for the moment of inertia). In presence of the free surface, the added mass of a floating object should vary depending also on the current configuration (Brennen, 1982). For simple geometries, the added mass can be calculated analytically, when a potential fluid flow (irrotational velocity field) is considered (Wendel, 1956).

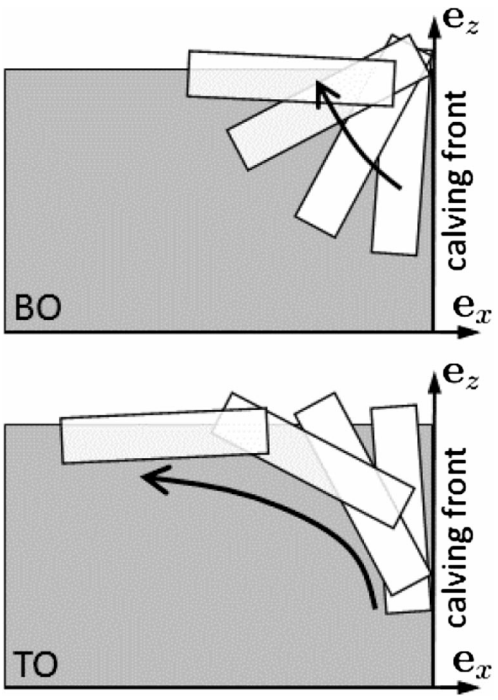

Figure 3. For BO calving events, hydrodynamic forces push the upper right iceberg tip against the calving front. For TO events, they make the iceberg move naturally away from the calving front.

In their model, Tsai et al. (2008) neglected the vertical added mass, considering only a horizontal added mass depending on the iceberg dimensions and inclination θ, and reasonably took a constant added moment of inertia that depended on the iceberg dimensions. Undoubtedly, the added mass improves the model and affects the capsize dynamics; however, solely it is not sufficient to capture it correctly nor to reproduce the difference between BO and TO events, which remain indistinguishable in that model. In our finite-element model, it is possible to add a varying added mass independently in *x*- and *z*-directions, but since we deal only with the displacement degrees of freedom, it is impossible to introduce independently the added moment of inertia. Therefore, to preserve the consistency of the model and to keep it as simple as possible, we decided not to take added mass into account.

Amundson, Burton, et al. (2012) did not take into account the added mass neither; however, they accounted for the drag force and torque. The authors approximated the hydrodynamic drag by forces and a torque applied to the iceberg center of mass and proportional to the corresponding squared linear and angular velocities weighted with drag coefficients, which are assumed to be constant over time. The components of the drag force depend only on the velocity of the center of mass $\dot{x}_G$ and $\dot{z}_G$, and the drag torque depends only on the rotation rate $\dot{\theta}$. Along each direction, the authors introduce a constant damping factor, which is estimated by fitting the model to laboratory experiments of capsizing centimeter-scale plastic blocks. However, since laboratory experiments involve much smaller Reynolds numbers than kilometer-size icebergs, we believe that the direct upscaling of lab results to field dimensions can be not straightforward. Moreover, as drag coefficients may vary with iceberg dimensions and shape, application to various iceberg morphologies requires an extra calibration step which would require additional experimental studies. More importantly, the horizontal drag force does not depend on the vertical velocity nor on the inclination θ the difference between BO and TO events, like the model proposed by Tsai et al. (2008). The difference in iceberg characteristics and calving style could be only captured if using different sets of empirical drag coefficients for the two types of events.

The model proposed in our study differs from the existing models by a potentially more accurate drag forces, which result from locally determined drag pressures computed over submerged parts. The main advantage is that since our model is incorporated in the finite-element framework, it can be used for floating and interacting deformable solids. The advantage of the locally defined drag pressure is that the resulting drag force and moment depend not only on the velocity of the center of mass and iceberg rotation rate, the local velocity of the submerged surfaces. Thus it naturally depends on the current iceberg position and tilt with respect to the free water surface. Such a coupling results in different drag effects for TO and BO events. Therefore, our model is able to reproduce the experimentally observed difference between BO and TO events even without introducing an ice-mélange effect as in Tsai et al. (2008). Indeed, as illustrated in Figure 3, hydrodynamic effects make BO and TO events asymmetrical. This can be easily understood for icebergs with small aspect ratios (Amundson, Burton, et al., 2012; Burton et al., 2012; MacAyeal et al., 2003). To minimize the dissipation due to the pressure drag, an initially TO-oriented iceberg, while it rises, tends to flow away from the terminus following a trajectory with minimal water resistance. On the other hand, for BO-oriented icebergs, the "minimal-resistance" trajectory will push the iceberg toward the calving front as it rises, thus forcing the iceberg to remain in contact with the front. Therefore, BO events last longer than TO events. This difference is not captured by the models of Tsai et al. (2008) and Amundson, Burton, et al. (2012) essentially because either the lack of the drag force or the lack of coupling of, horizontal motion, inclination angle, and drag forces in its evaluation, respectively.

It is worth highlighting that our model for fluid-structure interaction remains approximative (as well as other aforementioned models) and cannot be considered as ultimate capsize model. Nevertheless, we believe that it is accurate enough and in some aspects more accurate that those which were used before for the analysis of iceberg capsize. Obtaining a more accurate iceberg dynamics, would require solving Navier-Stokes equations

Table 2
Force Amplitudes and Timescale Responses to Tipping Iceberg Parameters

Quantity	Notation	Unit	Bottom-out	Top-out
Force linear density	F_c	N/m	$7 \times 10^6 - 6.9 \times 10^7$	$8.2 \times 10^6 - 7.3 \times 10^7$
Total force	LF_c	N	$3 \times 10^9 - 3.5 \times 10^{11}$	$4.1 \times 10^9 - 3.7 \times 10^{11}$
Force magnitude[a]	A	kg·m	$3 \times 10^{12} - 9.9 \times 10^{14}$	$5.7 \times 10^{12} - 8.2 \times 10^{14}$
CSF magnitude[b]	A_{CSF}	kg·m	$6 \times 10^{11} - 1.4 \times 10^{14}$	$5.6 \times 10^{11} - 2 \times 10^{14}$
Duration of the force	T	s	100–300	100–250

Note. CSF = centroid single force.
[a]From the double-integration in time of $F_c(t)$. [b]From the double-integration in time of CSF models that best fit $F_c(t)$ when filtered in the seismic band.

in presence of a free surface and contacting solids, which is a topic at the forefront of Computational Fluid Dynamic research, and thus beyond the present study. The simple model proposed here permits to carry out a parametric study and generate an accurate enough catalog of forces produced by iceberg capsize, which is one of the objectives of the current study.

3. Capsize Dynamics and Generated Forces

Below, we present results obtained for bottom-out (BO) and top-out (TO) capsize simulations for different aspect ratios, sizes and initial vertical positions of icebergs. A summary of possible force and duration ranges is presented in Table 2. We discuss the relation between capsize dynamics and the contact force generated on the glacier terminus and we compare the calculated force magnitudes with the ones inverted from glacial earthquake events.

3.1. Iceberg Motion and Energy

Figure 4 shows the time series of the iceberg position $\theta(t)$, $x_G(t)$ and $z_G(t)$, the iceberg potential energy E_{pot} and kinetic energy E_{kin} , and the horizontal contact force $F_c(t)$. Results are presented for BO (left) and TO (right) capsizes of an iceberg with aspect ratio $\epsilon = 0.2$ and height $H = 800$ m and which is initially neutrally buoyant ($\Delta z = 0$). Corresponding illustrative movies are available in the supplementary material (Movies S1 and S2). Capsize dynamics is different for different calving styles. For both BO and TO capsizes, the maximum kinetic energy is significantly lower (more than one order of magnitude) than the total gravitational potential energy that is released. The ratio of maximum kinetic energies BO/TO is ~0.4, which is in good agreement with the measurements of Amundson, Burton, et al. (2012) for plastic blocks of aspect ratio $\epsilon = 0.25$. Note that E_{kin} is the same for BO and TO rotations if the drag is not accounted for (black dashed lines in Figure 4b). In contrast, the E_{kin} calculated with the drag is about 6 times smaller than that calculated without drag for BO capsize, and about 3 times smaller for TO capsize. This shows that pressure drag has a stronger effect on BO than on TO iceberg capsize style. The differences between BO and TO capsizes come from the presence of the wall and related hydrodynamics, as detailed in section 2.2.3. This supports the observations made by Burton et al. (2012) and Amundson, Burton, et al. (2012) of energy dissipation measured in laboratory experiments for BO and TO events.

3.2. Force History

From the onset of capsize, the contact force (black lines in Figure 4c) increases, reaching a maximum for angle θ_M, and then decreases with a higher rate until loss of contact at θ_C. This results in smoothed-triangle like shaped horizontal force with dominant spectral content below 0.1 Hz. The red lines in Figure 4c represent forces after band-pass filtering in the glacial earthquake frequency band. We used a zero-phase Butterworth filter with corner frequencies 0.01 and 0.1 Hz. Filtered forces exhibit changes of their amplitude polarity at approximately the time of the loss of contact, called the *centroid time* and denoted by t_c. The waveform of the filtered force can then be roughly approximated by a centroid single force model (CSF, thick red line in Figure 4c), which is the source model commonly used in glacial earthquake seismic wave modeling (Tsai & Ekström, 2007; Tsai et al., 2008; Veitch & Nettles, 2012). For both BO and TO capsizes, 0.01- to 0.1-Hz filtered forces have lower amplitudes than the actual forces (by a factor larger than 2 here). This factor obviously depends on the frequency band of the filter and also on the frequency content of F_c that varies with calving style, iceberg dimensions and initial buoyancy conditions, as discussed later.

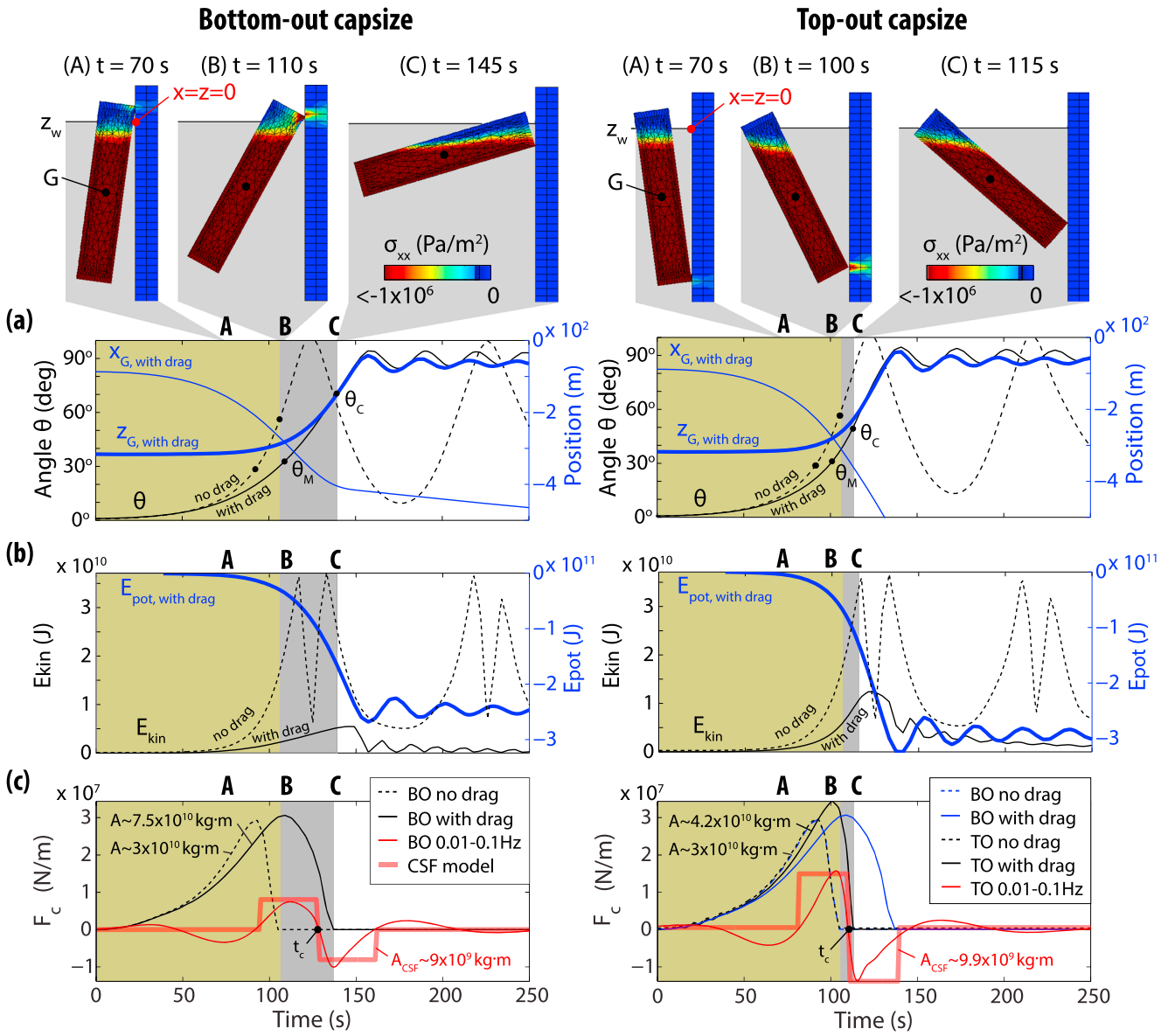

Figure 4. Results of bottom-out (left) and top-out (right) capsize simulations for an iceberg with $\epsilon = 0.2$ and $H = 800$ m. Top images illustrate capsize motions at different time steps: (A) when the iceberg is accelerating, (B) when the contact force with the wall is maximum, and (C) when at the loss of the iceberg-wall contact. The color scale represents the stress component σ_{xx} and is saturated beyond -1×10^6 Pa, to simplify the illustration. Variations with time of (a) angle of rotation (θ, black curve) and coordinates x_G and z_G of the center of mass G (blue), (b) iceberg kinetic (E_{kin} , black) and potential (E_{pot} , blue) energies, and (c) horizontal force density (F_c, black) and corresponding 0.01-0.1 Hz band-pass filtered force (red). The red thick curve shows the CSF model that best fits the force in the seismic band. In each graph, dashed curves represent time series of θ, E_{kin} and F_c when water drag is not accounted for. Gray-shaded boxes indicate the time range when the iceberg is in contact with the wall (i.e., $F_c > 0$ N and $\theta \leq \theta_C$). Same for yellow boxes but for capsize simulations without drag. θ_M and θ_C in (a) indicate the angles for maximum contact force and loss of iceberg/wall contact, respectively.

Iceberg capsize is a slow process which thus generates long-period seismic waves. Glacial earthquakes are generally observed to have dominant seismic frequency around 0.015–0.02 Hz (Tsai & Ekström, 2007). The depletion in high-frequency energy of glacial earthquakes (>1 Hz) is not a seismic wave propagation effect, but is produced by the source mechanism itself (Ekström et al., 2003). The lower-frequency corner of the band limitation should be related to the source duration. However, it is difficult to distinguish discrete seismic signals at frequencies below 0.01 Hz from other strong continuous noise or other calving-generated phenomena (Amundson, Clinton, et al., 2012; Sergeant et al., 2016; Walter et al., 2013). That is why we will refer to filtered forces between 0.01 Hz and 0.1 Hz for interpreting glacial earthquakes.

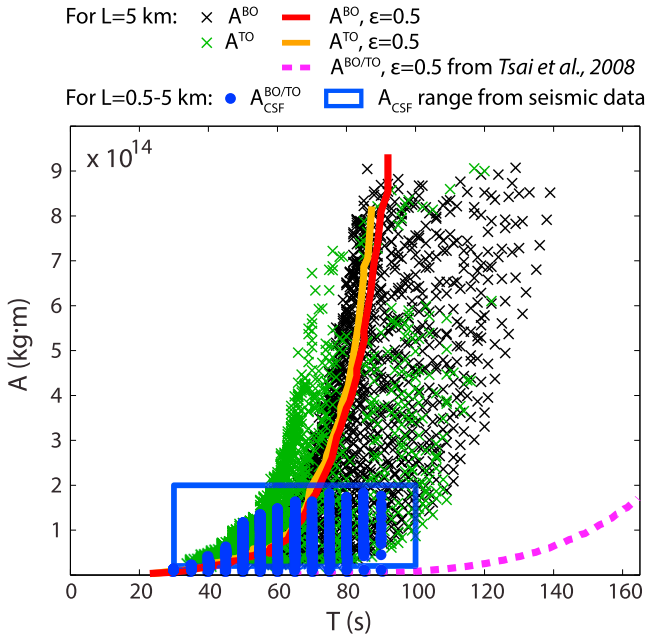

Figure 5. Force magnitudes A (kg·m) versus durations T' which corresponds to the effective duration of the force. Crosses are for BO (black) and TO (green) capsizes with iceberg height H = 100–1,000 m, aspect ratio $\epsilon = 0.1 - 0.7$ and length L = 5,000 m. Red and orange curves are for the specific value $\epsilon = 0.5$, for BO and TO, respectively. The pink dashed curve indicates the results of Tsai et al. (2008) for the same iceberg dimensions, BO and TO together. Blue points are CSF magnitudes A_{CSF} computed by integrating twice the CSF models that fit the 0.01- to 0.1-Hz filtered forces generated by BO and TO capsizes of icebergs with lengths varying between 500 and 5,000 m. Computed A_{CSF} values are in the range of seismic observations (blue box) derived from glacial earthquake CSF inversions (Tsai & Ekström, 2007; Veitch & Nettles, 2012).

The simulated TO and BO forces are different. The TO capsize is more rapid than the BO capsize presented here resulting in a shorter TO force duration T (T^{TO} = 115 s and T^{BO} = 145 s). The TO force reaches its maximum at $\theta_M \approx 30°$ and is released when $\theta_C \approx 48°$. For the BO case, $\theta_M \approx 32°$ and $\theta_C \approx 70°$. This results in a TO force that increases more rapidly to its maximum value than the BO force and then decreases more abruptly to zero. As a result, capsize of a given iceberg will produce different seismic signals depending on whether it capsizes in BO or TO style. As discussed above and concluded in the experiments of Amundson, Burton, et al. (2012), the difference between the forces generated by these two capsize styles comes from hydrodynamic effects. Indeed, when no pressure drag is accounted for (dashed lines in Figure 4c), BO and TO horizontal forces are identical.

3.3. Impact of Hydrodynamics on Force Magnitude and Comparison With Seismic Inversion

For the sake of consistency with previous studies (Tsai et al., 2008; Veitch & Nettles, 2012), we compute the so-called magnitude A by integrating the force history $F_c(t)$ twice:

$$A = \int_0^{T'} \int_0^{t} F_c(t')dt'dt. \tag{5}$$

The quantity A has units of kg·m and can represent a product mass × displacement for the iceberg or the calving glacier. Results are presented for iceberg aspect ratios $0.1 \leq \epsilon \leq 0.7$, heights 500 m $\leq H \leq$ 1,050 m, and lengths 500 m $\leq L \leq$ 5,000 m. These dimensions correspond to icebergs that can capsize spontaneously and that have the full glacier thickness (e.g., Amundson et al., 2008; Bamber et al., 2001) and an across-glacier length that does not exceed average glacier width in Greenland.

Figure 5 shows simulated magnitude A as a function of the effective force duration T' for BO (black crosses) and TO (green crosses) capsizes when L = 5,000 m. Note that the duration of the force generated during the entire capsize process ($T_{\theta_0 - \theta_c}$) strongly depends on the iceberg initial tilt θ_0: the smaller θ_0 is, the longer it takes to initiate the capsize, resulting in a smoother increase of the force. To get rid of this θ_0-dependency, here we define T' values as the duration for which the force rate $\dot{F}_c(t)$ is above the 20% threshold of the maximal force rate: $|\dot{F}_c| \leq 0.2 \max(|\dot{F}_c|)$. Orange and red lines represent the evolution of $A(T')$ for TO and BO icebergs with $\epsilon = 0.5$ and L = 5,000 m, respectively. We find significantly different results from those obtained with the model of (Tsai et al., 2008; dashed pink line, see also their Figure 7) in which no drag was used. Comparisons between our modeling results and those of Tsai et al. (2008) demonstrate the importance of water drag for capturing and discriminating BO and TO capsize dynamics. Accounting for drag forces results in higher magnitudes A compared to those computed without drag (Figures 4 and S1), especially for thin icebergs. These results are in good agreement with the observations of Amundson, Burton, et al. (2012, Figure 5b).

Finally, to interpret glacial earthquakes, we have to investigate the capsize response in the seismic band. For direct comparison to the source parameters inverted from seismic records, we compute the CSF magnitudes A_{CSF} by integrating twice the CSF models that best-fit the 0.01- to 0.1-Hz filtered force histories. Blue dots in Figure 5 indicate lower and upper boundaries for A_{CSF} values calculated from our simulations with varying L. We find A_{CSF} values that range between 5.6×10^{11} and 2×10^{14} kg·m. From the inversion of 300 events in Greenland, Tsai and Ekström (2007) and Veitch and Nettles (2012) find a range of A_{CSF} between 2×10^{13} and 2.1×10^{14} kg·m (blue box in Figure 5), the lower bound being associated with detection limits. Our modeling results are therefore in very good agreement with seismic observations. Without introducing an ice-mélange effect, they indicate that icebergs capsizing against the calving front generate a force compatible with glacial earthquake generation.

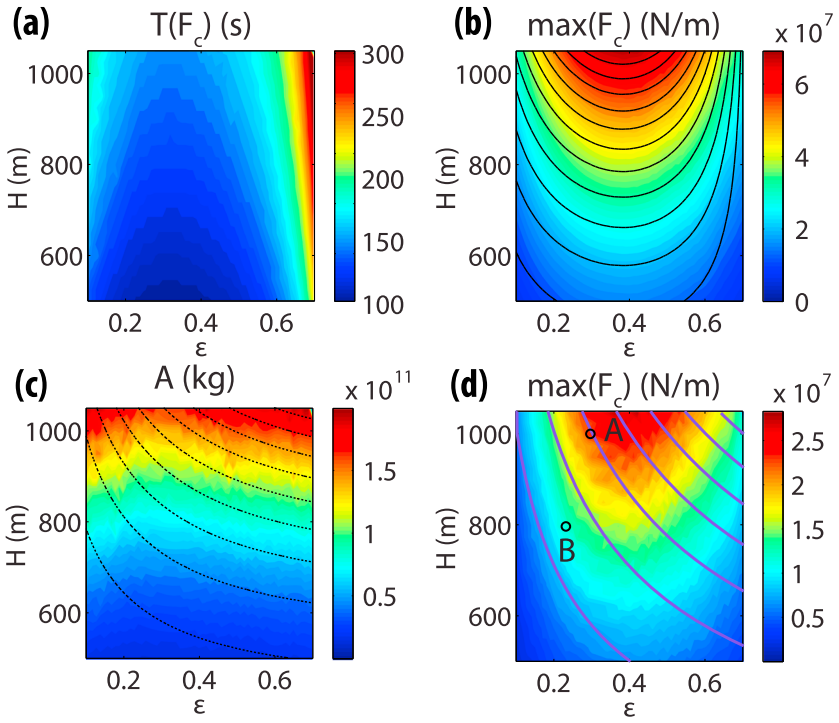

Figure 6. Variations of the BO contact force (a) duration T, (b) maximum amplitude, and (c) magnitude A with iceberg dimensions H and ϵ. Results are for the force linear density, which is equivalent to the forces of icebergs with $L = 1$ m. Panel (d) shows the force amplitude variations when filtered in the seismic band 0.01–0.1 Hz. Contour black curves on (b) show the analytical function $H^{2.6}\epsilon(\sqrt{1-\epsilon^2}-\epsilon)$ for the maximum amplitude of F_c . Contour black curves on (c) show the analytical function of the contact force magnitude $A \propto H^3\epsilon(\sqrt{1+\epsilon^2}-\epsilon)$ when hydrodynamic effects are not accounted for (Amundson, Burton, et al., 2012; Tsai et al., 2008). The purple contours on (d) show lines along which the iceberg volume $\epsilon H^2 L$ is constant. Black circles A and B indicate the iceberg dimensions and force magnitudes or amplitudes derived from seismic inversions of two glacial earthquakes (see text for details).

4. Force Variations With Iceberg Dimensions (ϵ, H)

We investigate now the sensitivity of the force (duration, maximum amplitude, magnitude, and force history) to iceberg dimensions (aspect ratio ϵ and height H) during BO and TO capsize events.

4.1. Bottom-Out Capsize

Figure 6 shows the (a) actual duration T and (b) maximum amplitude of the force as a function of ϵ and H. Here T is the actual duration of the force (equal to $T_{\theta_0-\theta_c}$) in contrast to T' which was introduced before to describe the effective duration of the significant force to be compared with results of Tsai et al. (2008). T ranges between 100 and 300 s meaning that the BO capsize process (from $\theta = 1° - 90°$) can last in the field up to 6 min as reported in Amundson et al. (2008) and Walter et al. (2012).

For a fixed aspect ratio, both force duration and amplitude increase with iceberg height. By best fitting the results for a given ϵ, we find that T roughly scales as H^α with α varying between 0.65 and 0.75 for different aspect ratios. The force duration and maximum amplitude distributions look approximately symmetric around a given ϵ_0. For every height H, T is minimum at $\epsilon_0 \approx 0.35$. Similarly, the contact force is maximum at $\epsilon_0 \approx 0.4$. The latter observation is in good agreement with analytical solutions proposed by (Amundson et al., 2010; Burton et al., 2012; MacAyeal et al., 2003). This means that the same force amplitude can be reached for two capsizing icebergs of same height and different $\epsilon \approx 0.4 \pm \Delta\epsilon$, where $0 < \Delta\epsilon \leq 0.3$. We find that the relative variations of the force amplitude with iceberg dimensions can be approximately fitted with the function $H^{2.6}\epsilon(\sqrt{1-\epsilon^2}-\epsilon)$ (black contour lines in Figure 6b), except when ϵ is close to its critical value for spontaneous iceberg capsize ($\epsilon \simeq 0.75$).

Figure 6c shows the distribution of the force magnitude A with iceberg dimensions. One obtains that A is weakly sensitive to the aspect ratio but essentially depends on H. As a consequence, the estimate of the iceberg volume from the contact force magnitude would then lead to significant uncertainties. Also shown

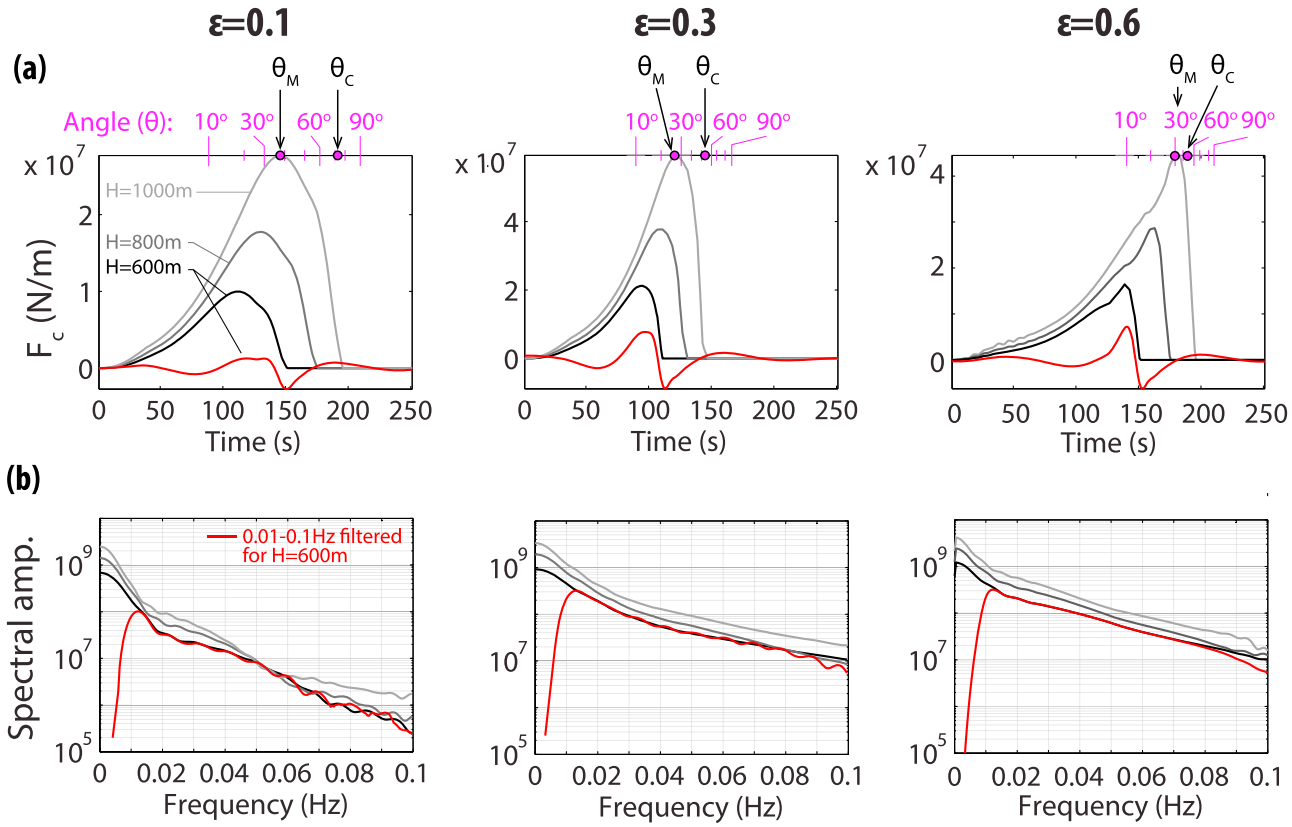

Figure 7. (a) Variations of the force history for three BO iceberg heights H = 600, 800, and 1,000 m, and aspect ratios ϵ = 0.1, 0.3, and 0.6. The red curves show the 0.01- to 0.1-Hz filtered forces for H = 600 m. The rotation angle θ for 1,000-m-high iceberg capsizes are indicated in purple at the top of each panel. (b) Variations of spectral amplitudes with frequency, associated with each modeled force.

on figure 6c (black dashed contour lines) is the analytical function $A \sim H^3\epsilon(\sqrt{1+\epsilon^2} - \epsilon)$ obtained by Amundson, Burton, et al. (2012) and Tsai et al. (2008) when no hydrodynamic effects are accounted for. This latter behavior, recovered by our modelling if drag is not considered, significantly departs from results with drag. This highlights large effect of drag forces and their parametrization.

When filtered in the seismic band (Figure 6d), the dependency of the maximum force amplitude on (ϵ, H) looks similar to that of the nonfiltered case even though it is no longer really symmetric with respect to $\epsilon \simeq 0.4$, especially when $H \geq 700$ m. This analysis clearly shows the tradeoff between ϵ and H, that is, several pairs (ϵ, H) can lead to the same force duration, amplitude or magnitude. It confirms the results of Tsai et al. (2008) and Amundson, Burton, et al. (2012) that the force magnitude (or amplitude) determined from seismic data cannot be used alone to discriminate and determine the iceberg size. To illustrate this, we have plotted lines of iso-volume $\epsilon H^2 L$, with L kept constant (purple contour lines in Figures 6d). For the same iceberg volume, the maximum force can vary up to 80%, depending on the combination of parameters ϵ and H.

To further provide a quantitative validation of the model, we compare computed 0.01- to 0.1-Hz force amplitudes and magnitudes A_{CSF} based on best-fitting CSF models to the values inverted for two glacial earthquakes (points A and B in Figure 6d) by Veitch and Nettles (2012) using the inversion method of Sergeant et al. (2016). Event A was generated by an iceberg with $L \approx$ 2,500 m, $H \approx$ 1,000 m, and $\epsilon \approx 0.3$ (volume 0.75 km^3), which calved BO from the Jakobshavn Isbrae glacier on 21 May 2010 (Rosenau et al., 2013). It produced a force of maximum amplitude 5.4×10^{10} N in the radial direction, normal to the terminus that is well reproduced by our model (computed maximum amplitude of 5.9×10^{10} N). Event B is due to the BO capsize of an iceberg with $L \approx$ 2,500 m, $H \approx$ 800 m, and $\epsilon \approx 0.23$ (volume 0.37 km^3) from Helheim glacier, on 25 July 2013 (Murray, Nettles, et al., 2015). It produced a force amplitude of 3×10^{10} N also very well reproduced by the proposed approach (amplitude of 2.95×10^{10} N).

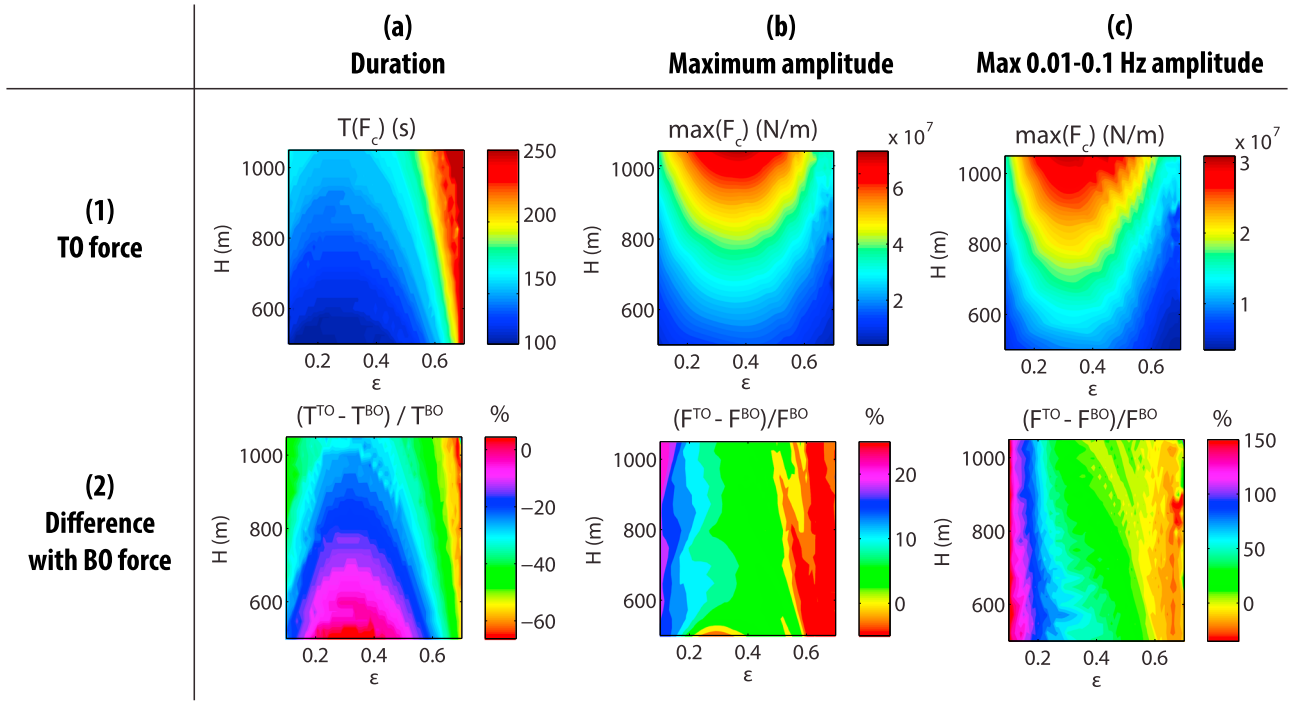

Figure 8. Top panels (1): Variations of the (a) duration T and (b–c) maximum amplitude of the force with ϵ and H, for TO events, when $L = 1$ m. Bottom panels (2): Same as in (1) but for the differences between TO and BO features, that is, $(F_c^{TO} - F_c^{BO})/F_c^{BO}$. Represented values are in percent. Positive (vs. negative) values indicate larger (vs. smaller) TO force amplitudes or durations, with respect to BO.

Let us now look in more details at the change in the force history (i.e., force shape) and associated spectral amplitudes, for iceberg aspect ratios $\epsilon = 0.1$, 0.3, and 0.6 and three different heights $H = 600$, 800, and 1,000 m (Figure 7). For a given aspect ratio, the amplitude and duration of the force increases with H but the shape of the force is similar for all H. On the contrary, when ϵ increases, the shape of the force changes with a sharper drop to zero when the iceberg loses contact with the terminus. The force shape is thus essentially controlled by ϵ as observed in laboratory experiments (Mac Cathles et al., 2015). More specifically, the capsize of thin icebergs ($\epsilon < 0.2$) exerts a long duration force on the terminus that slowly increases until its maximum at the rotation angle $\theta_M \approx 40°$ and then smoothly decreases until the loss of contact at $\theta_C \approx 80°$. For $\epsilon \geq 0.2$, force maxima are achieved for $\theta_M \approx 30°$ and the iceberg-to-terminus contact is lost at θ_C values decreasing from 70° to 40° as the aspect ratio increases.

The variability of the force history with ϵ then results in various spectra (Figure 7b). For $\epsilon < 0.2$, the spectral amplitudes decrease more rapidly with increasing frequency than when $\epsilon \geq 0.2$. This leads to much higher spectral ratios between low and high frequency components (LF/HF ratio) for thin icebergs. An important result of this analysis is that the change of the force shape with ϵ can be measured in the seismic frequency band (red lines).

4.2. Top-Out Capsize

The same analysis was carried out for TO events (Figure 8). As discussed in section 3, TO and BO capsizes yield identical forces when pressure drag is not accounted for. However, when the drag is accurately taken into account, the two forces differ since the calving front impedes the free rotation of the iceberg. The difference manifests in shorter TO capsize durations (up to 1.5 min) and therefore shorter TO force durations (100 s $\leq T \leq$ 250 s, Figure 8a first row).

The relative differences of the force maximum amplitude between TO and BO capsizes show that TO force amplitudes are always higher than those of BO, except for large icebergs with aspect ratios $\epsilon \geq 0.6$ (Figure 8b second row). This is especially true for $\epsilon < 0.2$, $F_c^{TO} \geq 1.2F_c^{BO}$ (i.e., an increase of 20% in the TO case). These large differences arise from hydrodynamic effects that are stronger for thinner icebergs (Figure S1). In the seismic band 0.01–0.1 Hz, the difference in the force maximum amplitudes is even higher, up to 150% (Figure 8b, fourth row). For example, $F_c^{TO} \geq 1.2F_c^{BO}$ at $\epsilon \sim 0.4$, and $F_c^{TO} \geq 1.8F_c^{BO}$ at $\epsilon \sim 0.2$. These differences are consistent

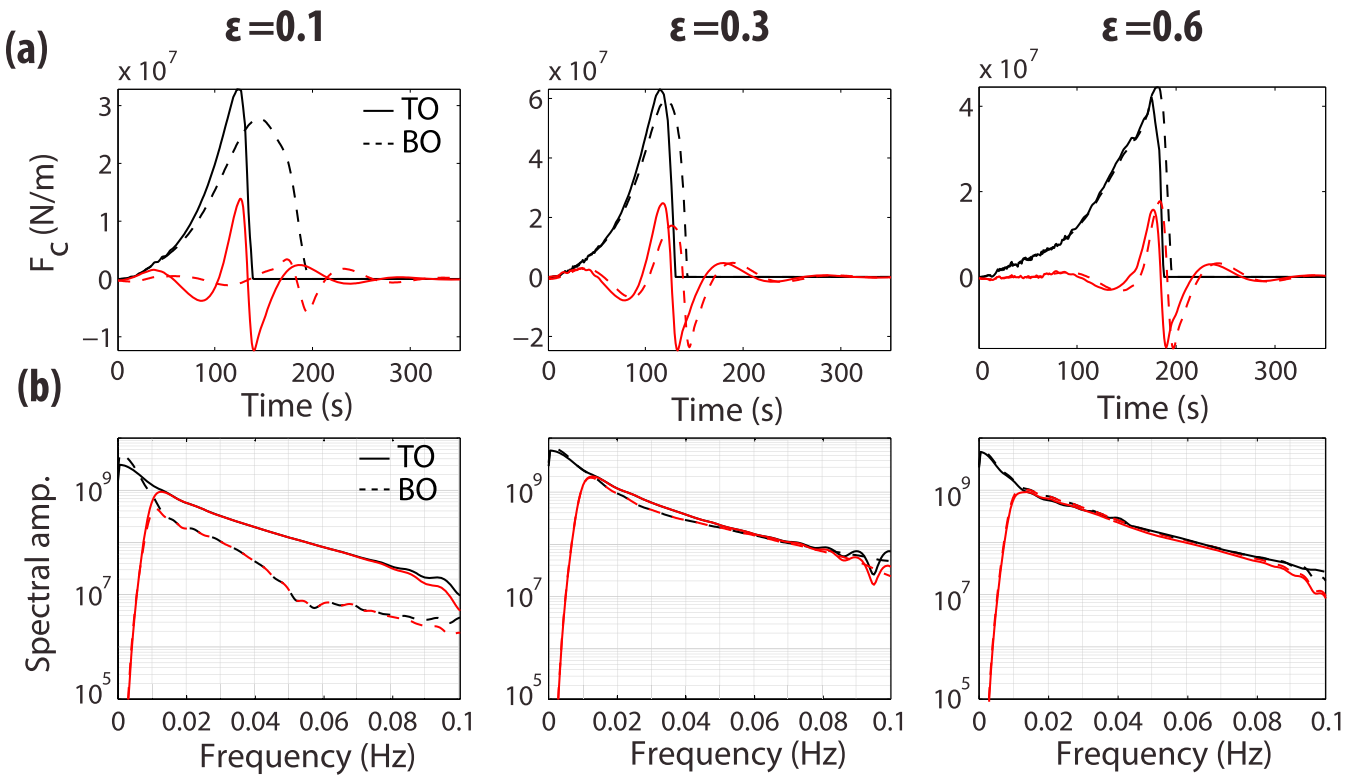

Figure 9. (a) Variations of the force history for TO (solid curves) and BO (dashed curves) iceberg capsizes with $\epsilon = 0.1$, 0.3 and 0.6 and $H = 1000$ m. The red curves show the 0.01- to 0.1-Hz filtered forces. (b) Variations of spectral amplitudes with frequency, associated with each force model.

with the observations of Sergeant et al. (2016) who determined inverted forces of similar amplitudes for a BO iceberg that was three times larger than the subsequent TO capsized iceberg along the same glacier terminus.

The very large variability of the maximum amplitude and duration of the force between TO and BO events, in the 0.01- to 0.1-Hz band, can be understood by looking at the differences of the shape and frequency content of the simulated force for different values of (ϵ, H). Figure 9 shows the force histories and associated spectral amplitudes for TO (solid lines) and BO (dashed lines) capsizes of icebergs with aspect ratios $\epsilon = 0.1$, 0.3, and 0.6. For the thinnest icebergs ($\epsilon \leq 0.2$), loss of iceberg contact with the wall occurs much earlier for TO capsizes than for BO capsizes ($\theta_C^{TO} \approx 55°$ and $\theta_C^{BO} \approx 80°$). The TO force has a higher amplitude and drops more sharply from its maximum to zero than the BO force. As the aspect ratio increases, TO and BO forces tend to resemble each other. Interestingly, for aspect ratio $\epsilon = 0.6$, the BO real and filtered forces are slightly higher than the corresponding TO forces. Note that the force shape of TO icebergs is less sensitive to ϵ than the BO force shape due to hydrodynamic effects.

5. Force Variations With Iceberg Initial Buoyant Conditions

The glacier terminus is not necessarily at its hydrostatic equilibrium, depending on the bedrock slope, water depth, and floating ice-tongue length (e.g., James et al., 2014; Murray, Selmes, et al., 2015; Rosenau et al., 2013; Wagner et al., 2016). If the iceberg that detaches from the calving front is not neutrally buoyant at the initiation of its capsize, it will experience up- or down-lift, possibly affecting its contact with the terminus. Those scenarios may happen if (i) the iceberg's height is smaller than the full-glacier thickness, and/or (ii) at the initiation of calving, mass loss occurs, triggered and associated with serac collapses or ice-avalanching along the calving front as it is often observed (Amundson et al., 2010; Sergeant et al., 2016), and/or (iii) at the time of the event, the terminus in the vicinity of the calving front is not neutrally buoyant. The latter scenario (iii) may occur for several reasons. On the one hand, ungrounded glacier termini show vertical oscillations in response to the ocean tidal forcing with a time lag of a few hours, particularly before calving (e.g., De Juan et al., 2010). On the other hand, fracture leading to the formation of a full-glacier thickness iceberg is a long process that can last up to 2 days (Xie et al., 2016). Meanwhile, the future ice block is likely to acquire a nonzero

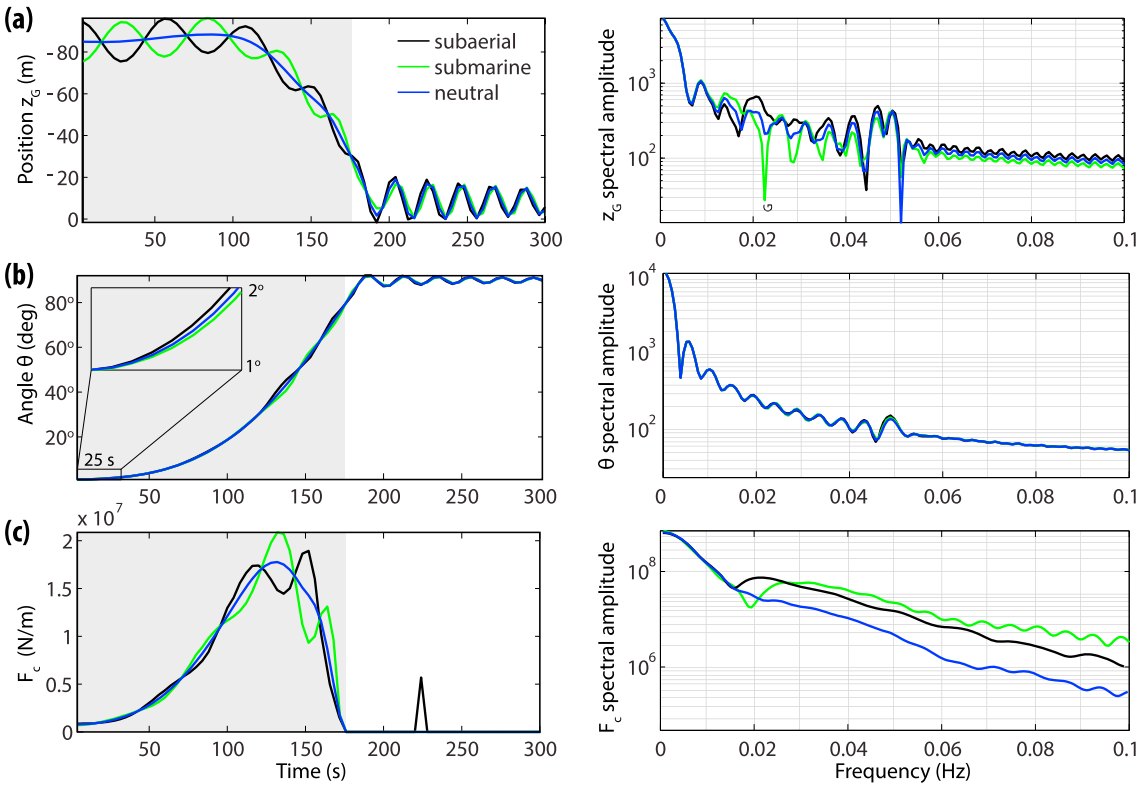

Figure 10. Time series of the (a) vertical positions $z_G(t)$, (b) angle $\theta(t)$, (c) horizontal force $F_c(t)$, and associated spectral energy distribution for submarine (green), subaerial (black), and initially neutrally buoyant (blue) capsizing icebergs. Results are for BO icebergs with $\epsilon = 0.1$, $H = 800$ m, and $|\Delta z| = 10$ m.

tilt angle (up to ~5°) that deviates its orientation from its initial vertical position. Murray, Selmes, et al. (2015) measured some anomalies of the Helheim terminus elevation close to the front, right before calving. The future portion of ice-to-be-calved showed a few-meter uplift before its release and bottom-out capsize, once the basal crevasses crossed the full-glacier thickness. Both modeling and field observations indicate that the glacier terminus can be outside its hydrostatic equilibrium with a few-meter difference with respect to its neutrally buoyant elevation.

We therefore investigate the change in the calving force associated with initial equilibrium of the iceberg by varying the water level around the iceberg buoyant state that occurs at water elevation z_w (hydrostatic equilibrium of the ice block). The perturbation of water level for an initial nonneutrally buoyant iceberg, $\Delta z = z_0 - z_w$, is varied within the range −10 to +10 m, where z_0 is the actual water level. Icebergs that experience a waterline with $\Delta z < 0$ and $\Delta z > 0$ are referred to as subaerial and submarine icebergs, respectively.

Figure 10 shows the time evolution and associated spectral amplitudes of the rotation angles $\theta(t)$, vertical positions $z_G(t)$ and contact forces $F_c(t)$ that are generated by the capsizes of a neutrally buoyant iceberg (blue lines), and a subaerial (black) or submarine (green) iceberg.

Figure 11 shows the force and associated spectral amplitudes for subaerial and submarine capsizing icebergs ($\epsilon = 0.1$, $H = 800$ m) for different Δz. Gray-shaded lines show that the higher $|\Delta z|$ (resulting in a higher buoyancy force), the more affected the capsize force is. Nonneutral icebergs exert a force on the terminus with higher spectral amplitudes at high frequencies, with respect to the neutral force (blue lines). We denote as f_{plus} and f_{gap} the central frequency of the peaks observed in the force spectra of nonneutrally buoyant icebergs corresponding to amplification and decrease of frequency content, respectively. Interestingly, for submarine icebergs, the amount of depleted energy at f_{gap} is very high. The spectral amplitude perturbations at f_{plus} and f_{gap} increases with $|\Delta z|$ and are maximum for icebergs of aspect ratios $\epsilon \sim 0.1$ and $\epsilon \geq 0.6$. Indeed, the dynamics of the thinnest and widest icebergs are much more affected by initial buoyant conditions as these ice blocks rotate more slowly than intermediate-ϵ icebergs (section 4.1 and Figure 6a). Values of f_{plus} and f_{gap} vary with ϵ and H within the range 0.012 to 0.03 Hz (see Text S1 and Figure S2).

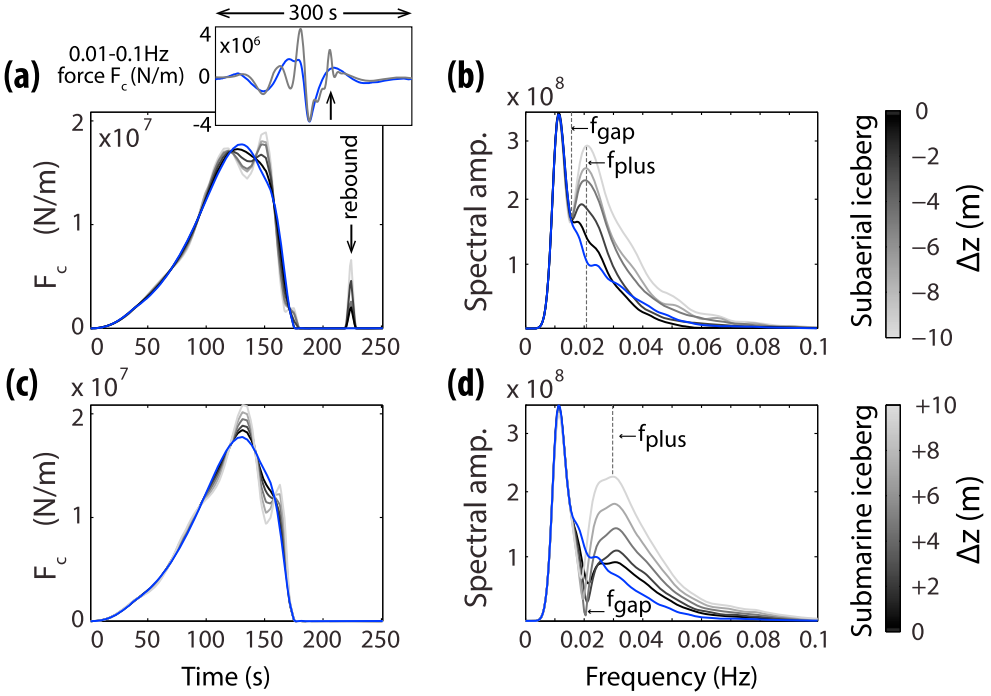

Figure 11. Effects of initial conditions for the hydrostatic equilibrium of the capsizing iceberg on the force (a and c) history and (b and d) spectral amplitudes. For more visibility, spectral amplitudes are for the 0.01- to 0.1-Hz filtered time series. The blue curves are results for neutrally buoyant icebergs (i.e., $\Delta z = 0$ m). The different shades of gray curves are results for different nonzero $|\Delta z|$ values. Top graphs (a–b) are for subaerial icebergs ($\Delta z < 0$). Bottom graphs (c–d) are for submarine icebergs ($\Delta z > 0$). Results are shown here for BO icebergs with $\epsilon = 0.1$, $H = 800$ m. The inset box above the top-left panel represents the forces filtered in the seismic band 0.01–0.1 Hz associated with the capsize of a neutral iceberg (blue curve) and a subaerial iceberg (gray curve). The black arrow indicates the seismic signature for the iceberg impact on the terminus, once it has fully capsized.

Note also that a pulse in the horizontal force for subaerial icebergs can be observed in Figure 11a, after the loss of contact with the terminus. This results from an impact of the iceberg on the wall after it has fully capsized (top left corner of the rectangular ice block, see Figure 1). This impact can affect the filtered force (inset box in the figure) depending on the band-pass filter corner frequencies and the delay ΔT between the loss of contact and the subsequent iceberg-to-terminus collision. We observe such impacts only for thin subaerial icebergs with aspect ratios $\epsilon \leq 0.12$ (at any Δz-value in the investigated range down to -10 m) and for submarine icebergs with $\epsilon \leq 0.15$ and for $\Delta z > 6$ m. ΔT ranges from 15 to 135 s after the loss of contact. This leads to a visible impact signature that is not necessarily distinguishable from the capsize force signal if the force history is low-pass filtered with a corner frequency below $1/(2\Delta T)$. For example, if the impact occurs 50 s after the loss of contact, the capsize and collision signals are distinguishable in the seismic band (≥ 0.01 Hz). For a ΔT of 20 s, the two sources cannot then be distinguished for frequencies below 0.025 Hz. Iceberg capsize and subsequent impact would then act like a unique seismogenic source.

Finally, note that the frequency gap due to the iceberg initial floatation level is also observed in the seismic records of glacial earthquakes and in the inverted forces. Figure 12 shows the results for the force histories and associated normalized spectrograms and power spectra from (a) our modeling and (b) waveform inversion of three glacial earthquakes recorded at GLISN broadband seismic stations (yellow triangles in inset maps). The data forces (red lines in (b)) were inverted following the method of Sergeant et al. (2016) in the band-pass frequency band 0.01–0.1 Hz for seismic events, which occurred on 2012/01/03 2012 11:11:41.7 UTC in Upernavik Isstrom; 2012/04/24 4:46:21.6 UTC in Rink glacier; and 2013/03/04 11:41:29.3 UTC in Helheim glacier. Glacial earthquake origin times and locations (red stars) were provided by Olsen and Nettles (2017).

Force spectra data (in red) shows specific frequencies (indicated by arrows in Figure 12) for maximum spectral peak, secondary peak, or spectral gaps that are well fitted with the model force spectra computed for subaerial or submarine icebergs (black lines). These features could not be reproduced when using initially neutrally

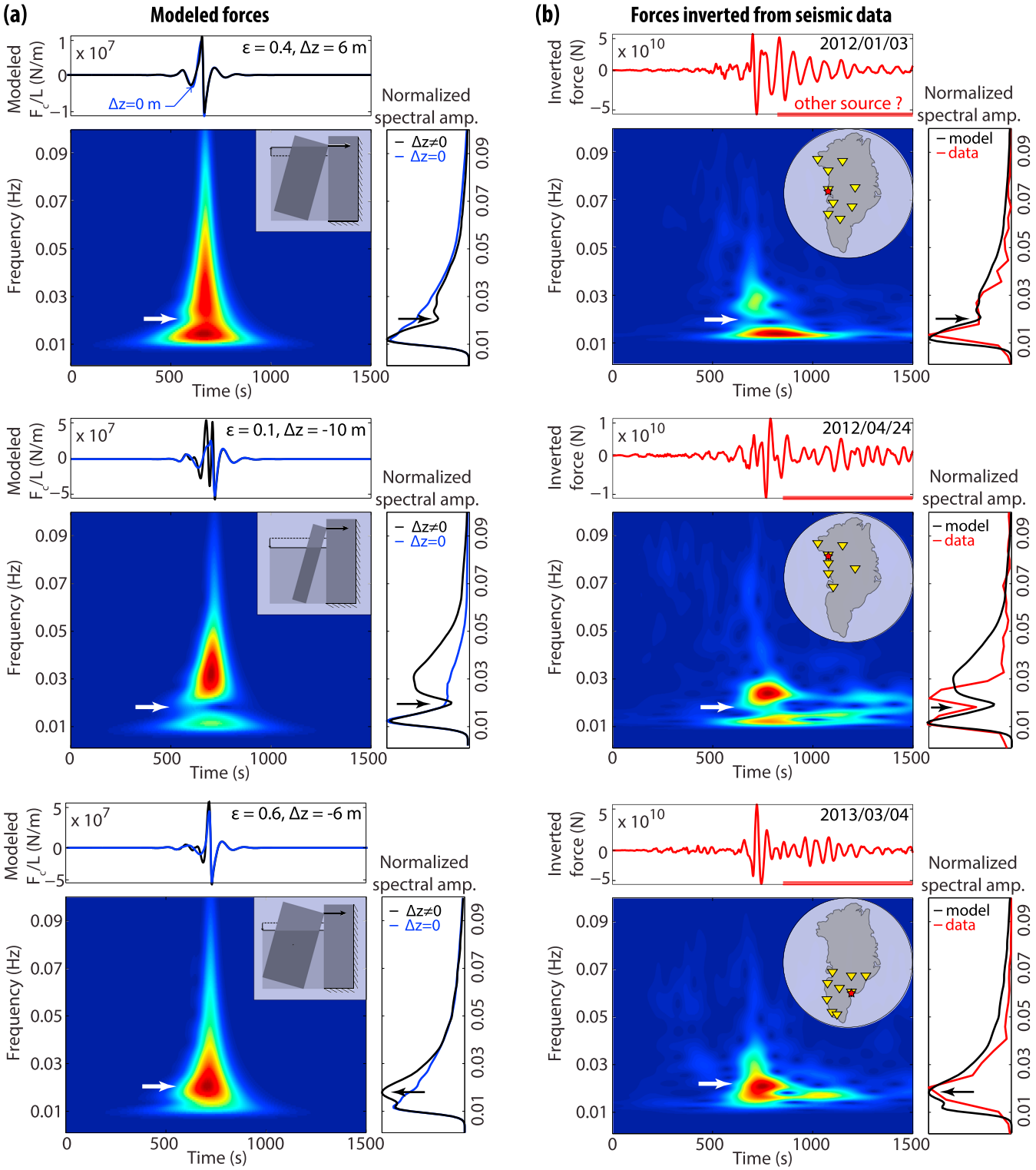

Figure 12. Comparison of the forces (a) simulated with iceberg capsize models and (b) inverted from seismic data, both filtered between 0.01 and 0.1 Hz, as well as the associated normalized spectrograms and power spectra. These simulated and inverted forces are for systems out of buoyant equilibrium (i.e., $\Delta z \neq 0$). For field data in Greenland (column (b)), locations of the calving events and GLISN stations used in the waveform inversion are indicated on inset maps by red stars and yellow triangles, respectively. The power spectra panels show the forces inverted from seismic data (red curves), modeled with either submarine or subaerial icebergs (black curves), and modeled with neutral icebergs (blue curves). The comparison between models and data show that seismic data spectral peaks or gaps indicated by arrows can be explained by the initial buoyant state of the capsizing icebergs, especially when they are out of their flotation level when they start calving.

buoyant icebergs (blue lines). As spectral gaps are observed at every Greenland station that has recorded the earthquakes, our study suggests that they are a real source effect for icebergs that calve from nonneutrally buoyant terminus fronts.

6. Concluding Remarks

This study presents a 2-D numerical model designed to investigate BO and TO iceberg capsize dynamics and the horizontal component of the force applied on the glacier terminus. The model accounts for iceberg-water interactions, ice rheology and frictional contacts. One difficulty of this modeling approach was to design an appropriate drag model to study large-scale capsize phenomena and in particular to capture the differences between BO and TO events. Though the present model for fluid-structure interaction remains approximative and cannot be considered as ultimate capsize model it permits to carry out a parametric study and generate an accurate enough catalog of forces produced by iceberg capsize.

We analyzed the variations of the force shape, amplitude and duration and the spectral energy distribution with iceberg dimensions (aspect ratio ϵ and height H), the initial buoyant conditions and calving style. We considered the actual iceberg-to-terminus contact force but also the horizontal force component band-pass filtered in the seismic band 0.01 – 0.1 Hz. This study provides catalogs for the horizontal force generated by the capsize of icebergs responsible for glacial earthquakes. Main results are as follows:

1. For a fixed aspect ratio, the force duration T, amplitude and therefore magnitude A increase with iceberg height H.
2. For a given height, similar force amplitudes are found for aspect ratios $\epsilon \approx 0.4 \pm \Delta\epsilon$ with $\Delta\epsilon$ a perturbation of ϵ.
3. The force time evolution (force shape) and its spectral energy distribution spectrum modulus differs with the initial state of equilibrium of the iceberg, the calving style and ϵ, especially for BO capsizes.
4. Force amplitudes and magnitudes related to BO and TO capsizes differ for icebergs of the same dimensions. Except for very wide icebergs ($\epsilon \geq 0.6$), TO icebergs exert an up to 20% larger force on the terminus than BO capsizes and, especially in the seismic band, TO force amplitude can be 1.5 larger than the BO 0.01- to 0.1-Hz filtered force. Conversely, wide TO icebergs ($\epsilon \geq 0.6$) exert a weaker force on the terminus.
5. For thin icebergs ($\epsilon \leq 0.12$), impact against the glacier terminus occurring at ΔT around 15 to 135 s after the loss of contact are observed in the simulation. In the studied case, the force exerted by this impact is of the same order of magnitude of the capsize force, and cannot necessarily be distinguished from the capsize force signal if the force history is low-pass filtered with a corner frequency below $1/(2\Delta T)$.

A key point, in line with former studies (Amundson, Burton, et al., 2012; Tsai et al., 2008), is that the contact force amplitude is not uniquely defined by the iceberg volume but depends on a combination of parameters ϵ and H, Δz and also on the calving style. This implies that glacial earthquake magnitude cannot be interpreted in terms of iceberg volume only, in order to characterize ice mass loss at individual glaciers. However, an important result is that the force history carries the signature of the iceberg geometry (H, ϵ), its initial buoyancy state Δz and its calving style. In particular, great differences in the force histories and spectra are obtained for varying distances Δz to the initial ice-block flotation level. The variability of the force spectral content shown in Figure 12 is qualitatively observed in the forces inverted from glacial earthquake when considering icebergs out of their hydrostatic equilibrium ($\Delta z \neq 0$).

An important point is that each of the parameters (ϵ, H, Δz) acts very differently on this force history. As a result, comparing the full force history inverted from seismic data to the catalog of forces calculated with our model may provide a way to determine the iceberg characteristics (ice mass loss) from the seismic signal as done for landslides. Indeed, for landslides, combining seismic inversion and numerical modeling makes it possible to determine the characteristics of the released mass and the friction coefficient and to quantify physical processes acting during the flow (e.g., erosion; Moretti et al., 2012; Moretti et al., 2015; Yamada, Mangeney, Matsushi & Moretti, 2018; Yamada, Mangeney, Matsushi & Matsuzawai, 2018). To reduce the number of possible (ϵ, H) combinations, one could possibly often assume that the iceberg heights are close to the glacier thickness in the margin of the calving front.

Finally, we derived force magnitudes that are consistent with seismic observations (Table 2). This contrasts with the results of Tsai et al. (2008) who obtained only order-of-magnitude agreement with glacial earthquake magnitudes for calving models without ice mélange. The presence of ice mélange may also influence calving

style and its effect on capsize dynamics and generated forces (Amundson et al., 2010; Tsai et al., 2008) should therefore be investigated in future work.

In addition, several features that may have consequences on glacial earthquakes have not yet been addressed, such as iceberg geometry (all studies so far have used box-shaped icebergs), complex hydrodynamics (turbulent flow, generated ocean waves), disintegration and collapse of icebergs while calving, the effect of ice mélange, and terminus conditions and their implications for the glacier stability. At this stage, the model is limited to a configuration involving a fixed wall that does not have any floating part. For this reason, we did not compute the vertical force resulting from glacial earthquakes, which has so far been attributed to co-seismic glacier bending (Murray, Nettles, et al., 2015). Investigating the vertical force component generated during the process of iceberg capsizing against an ungrounded terminus should help in the characterization of glacier ice-ice friction, the discrimination of BO from TO events and the refinement of our understanding of the cause of glacial earthquakes.

Appendix A: Justification of the Drag Model

The proposed drag model is phenomenological, as it is based on the assumption that pressure drag scales as squared velocity of the moving solid, as in Amundson, Burton, et al. (2012) but is integrated locally. This remains of course a big assumption but in our case, the drag is only needed to be able to simulate the damping of the solid in fluid. To justify the choice for the used local fluid effect model, we discuss below the dependency of the friction drag on the Reynolds number and we compare pressure drag computations based on equation (3) with experimental data on a simple case study.

The effective drag force $F_D = F_{D_p} + F_{D_f}$ and associated moment M_D exerted on the iceberg are estimated by integrating the pressure and friction drags over the submerged surface. Experimental measurements of water drag exerted on a cylinder moving at variable speed show that the friction drag to total drag ratio F_{D_f}/F_D is small and decreases with the Reynolds number: F_{D_f}/F_D is 0.138, 0.0483, and 0.0158 for $Re = 10^3$, 10^4, and 10^5, respectively (Munson et al., 2012, p. 516). For a kilometer-scale capsizing iceberg, the Reynolds number is of the order of 10^{11}, and therefore, the drag exerted on the ice block may be essentially due to pressure drag. This observation is also supported by the trajectory of icebergs in the open ocean: the drift at slow velocities of kilometer-size icebergs in sea currents ($Re \approx 10^9$) is well modeled when a very small amount of friction drag is included (Smith & Banke, 1983). Thus, we model here iceberg capsize dynamics with the pressure drag only.

To justify the choice of the local drag pressure, we compare pressure drag computations based on equation (3) with experimental data. We compute drag coefficients $C_D = \frac{F_D}{0.5\rho_w V^2 A}$ for ellipsoidal bodies with different aspect ratios b/a, where V is the body velocity relative to the fluid and $A = La$ the area of a vertical cross section passing through the center of the ellipse. The computed values of C_D are compared to experimental

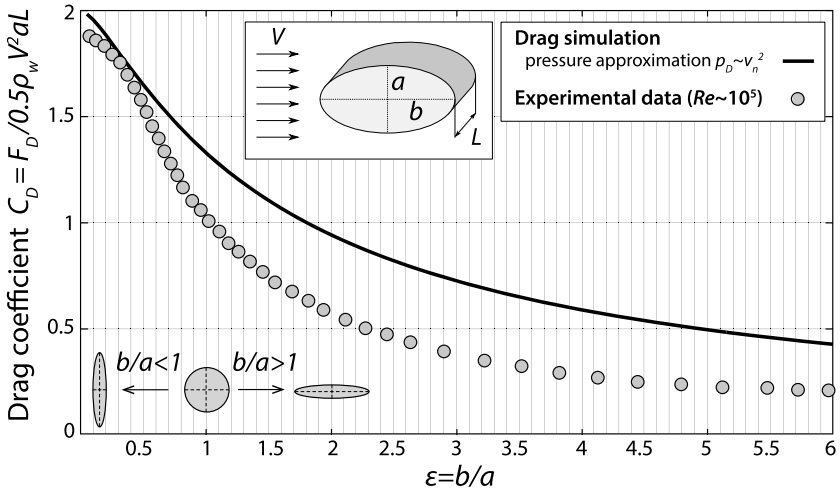

Figure A1. Drag coefficients C_D computed with the pressure drag approximation from equation (3) (solid curve) and experimental measurements (circles) from Munson et al. (2012). Results are for ellipses of various aspect ratios b/a (semiaxes a and b) moving in water with relative velocity V at $Re \sim 10^5$.

measurements extracted from Munson et al. (2012) at $Re = 10^5$ (Figure A1). The model well captures the qualitative evolution of the drag coefficient and provides relatively accurate quantitative results at small aspect ratios $\epsilon \leq 0.7$, which are the aspect ratios of interest for the rectangular icebergs considered in this study. For larger aspect ratios, the discrepancy is larger but the hydrodynamics around smooth solids elongated along the flow direction can be considered irrelevant to flows near the capsizing icebergs.

Note that, as friction drag is not taken into account in the proposed framework, the laboratory-scale experiments of Amundson, Burton, et al. (2012) cannot be reproduced with our model as these experiments involved much smaller Reynolds numbers than those of kilometer-size capsizing icebergs. Capsize dynamics are probably affected by a nonnegligible portion of viscous drag.

Appendix B: Sensitivity of the Model to the Ice-Ice Friction Coefficient

Concerning contact forces, in a real iceberg-terminus contact, the processes involved might be complex given that the surfaces in contact are not flat, that water should act as a lubricant, and that the ice may break at some locations. Inversion of seismic records gives the forces applied by the iceberg to the terminus, with inclination angle δ always smaller than 30° and usually below 10° (Tsai & Ekström, 2007). This leads to vertical-to-horizontal force ratios $F_z/F_x = \tan\delta$ lower than 0.58 and 0.18, respectively. If we assume that the vertical force component comes from frictional shear on the calving front only, the ice-ice global friction coefficient should generally satisfy $\mu < 0.18$. On the other hand, the value of ice-ice friction is highly variable depending on the sliding velocity and temperature (e.g., Schulson & Fortt, 2012). Oksanen and Keinonen (1982) measured a small value of the kinetic friction $\mu < 0.05$ for a range of velocities between 0.5 and 3 m/s and temperature close to the melting point (−2 °C), primarily due to friction-generated heat and local ice melting. Our modeling results indicate that, for kilometer-scale icebergs, the relative sliding velocity v_s is lower than 5 m/s. Oksanen and Keinonen (1982) further show that μ increases as a function of $v_s^{1/2}$. However, the extrapolation of dry ice-ice experiment measurements to the field environment and glacier front conditions is clearly a difficult task and therefore μ can be considered to be an unconstrained parameter within a range of small values. Here, for the sake of simplicity, we use a constant friction coefficient. We ran several computations under the conditions given in section 2. Testing the effect of μ values in the range 0–0.1, we find that a 0.05 increase of μ leads to a small decrease of the force amplitude and a negligible rise of its duration, the change of both being less than 1%. We therefore use $\mu = 0$ in the following study (Table 1).

Acknowledgments
We gratefully acknowledge François Charru (IMFT) and Pauline Bonnet (IPGP) for enlightening discussions. The authors thank Olga Sergienko, Jason Amundson, Victor Tsai, and Brad Lipovsky for their review, which significantly helped to improve the manuscript. The numerical modeling was done using Z-set (www.zset-software.com), a nonlinear finite-element suite developed by the Centre des Matériaux, Mines ParisTech and Onera (France). Glacial earthquake detections and locations can be accessed from GlobalCMT (http://www.globalcmt.org/Events/). GLISN seismic data can be obtained from the IRIS DMC archive center (https://ds.iris.edu/ds). This work has been partially funded by ANR contract ANR-11-BS01-0016 LANDQUAKES, CNCS-UEFISCDI project PN-II-ID-PCE-2011-3-0045, Institut Universitaire de France and ERC contract ERC-CG-2013-PE10-617472 SLIDEQUAKES. The research was supported by a DGA-MRIS scholarship. This is IPGP contribution number 3989.

References

Amundson, J. M., Burton, J. C., & Correa-Legisos, S. (2012). Impact of hydrodynamics on seismic signals generated by iceberg collisions. *Annals of Glaciology*, *53*(60), 106–112.

Amundson, J. M., Clinton, J. F., Fahnestock, M., Truffer, M., Lüthi, M. P., & Motyka, R. J. (2012). Observing calving-generated ocean waves with coastal broadband seismometers, jakobshavn isbræ, Greenland. *Annals of Glaciology*, *53*(60), 79–84.

Amundson, J. M., Fahnestock, M., Truffer, M., Brown, J., Lüthi, M. P., & Motyka, R. J. (2010). Ice mélange dynamics and implications for terminus stability, jakobshavn isbræ, Greenland. *Journal of Geophysical Research*, *115*, F01005. https://doi.org/10.1029/2009JF001405

Amundson, J., Truffer, M., Lüthi, M., Fahnestock, M., West, M., & Motyka, R. (2008). Glacier, fjord, and seismic response to recent large calving events, jakobshavn isbræ, Greenland. *Geophysical Research Letters*, *35*, L22501. https://doi.org/10.1029/2008GL035281

Bamber, J. L., Layberry, R. L., & Gogineni, S. (2001). A new ice thickness and bed data set for the Greenland ice sheet: 1. Measurement, data reduction, and errors. *Journal of Geophysical Research*, *106*(D24), 33,773–33,780.

Besson, J., & Foerch, R. (1997). Large scale object-oriented finite element code design. *Computer Methods in Applied Mechanics and Engineering*, *142*(1), 165–187.

Brennen, C. (1982). A review of added mass and fluid inertial forces, NASA STI/Recon Technical Report N, 82.

Burton, J., Amundson, J., Abbot, D., Boghosian, A., Cathles, L. M., Correa-Legisos, S., et al. (2012). Laboratory investigations of iceberg capsize dynamics, energy dissipation and tsunamigenesis. *Journal of Geophysical Research*, *117*, F01007. https://doi.org/10.1029/2011JF002055

Castelnau, O., Duval, P., Montagnat, M., & Brenner, R. (2008). Elastoviscoplastic micromechanical modeling of the transient creep of ice. *Journal of Geophysical Research*, *113*, B11203. https://doi.org/10.1029/2008JB005751

De Juan, J., Elósegui, P., Nettles, M., Larsen, T. B., Davis, J. L., Hamilton, G. S., et al. (2010). Sudden increase in tidal response linked to calving and acceleration at a large Greenland outlet glacier. *Geophysical Research Letters*, *37*, L12501. https://doi.org/10.1029/2010GL043289

Ekström, G., Nettles, M., & Abers, G. A. (2003). Glacial earthquakes. *Science*, *302*(5645), 622–624.

Ekström, G., & Stark, C. P. (2013). Simple scaling of catastrophic landslide dynamics. *Science*, *339*(6126), 1416–1419.

Favreau, P., Mangeney, A., Lucas, A., Crosta, G., & Bouchut, F. (2010). Numerical modeling of landquakes. *Geophysical Research Letters*, *37*, L15305. https://doi.org/10.1029/2010GL043512

Francavilla, A., & Zienkiewicz, O. (1975). A note on numerical computation of elastic contact problems. *International Journal for Numerical Methods in Engineering*, *9*(4), 913–924.

Hilber, H. M., Hughes, T. J., & Taylor, R. L. (1977). Improved numerical dissipation for time integration algorithms in structural dynamics. *Earthquake Engineering & Structural Dynamics*, *5*(3), 283–292.

Howat, I. M., Joughin, I., & Scambos, T. A. (2007). Rapid changes in ice discharge from Greenland outlet glaciers. *Science*, *315*(5818), 1559–1561.

James, T. D., Murray, T., Selmes, N., & Scharrer, K. (2014). M. O Leary Buoyant flexure and basal crevassing in dynamic mass loss at helheim glacier. *Nature Geoscience*, *7*(8), 593–596.
Jean, M. (1995). Frictional contact in collections of rigid or deformable bodies: Numerical simulation of geomaterial motions. *Studies in Applied Mechanics*, *42*, 463–486.
Joughin, I., Abdalati, W., & Fahnestock, M. (2004). Large fluctuations in speed on Greenland's Jakobshavn Isbrae Glacier. *Nature*, *432*(7017), 608–610.
Krug, J. W. O. G. J., & Durand, G. (2014). Combining damage and fracture mechanics to model calving. *The Cryosphere*, *8*, 2101–2117.
Mac Cathles, L., Kaluzienski, L., & Burton, J. (2015). *Laboratory investigations of seismicity caused by iceberg calving and capsize*. Abstract C43B-0803 presented at 2015 Fall Meeting, AGU, San Francisco, Calif., 14–18 Dec.
MacAyeal, D. R., Scambos, T. A., Hulbe, C. L., & Fahnestock, M. A. (2003). Catastrophic ice-shelf break-up by an ice-shelf-fragment-capsize mechanism. *Journal of Glaciology*, *49*(164), 22–36.
Montagnat, M., Castelnau, O., Bons, P., Faria, S., Gagliardini, O., Gillet-Chaulet, F., et al. (2014). Multiscale modeling of ice deformation behavior. *Journal of Structural Geology*, *61*, 78–108.
Moretti, L., Allstadt, K., Mangeney, A., Capdeville, Y., Stutzmann, E., & Bouchut, F. (2015). Numerical modeling of the Mount Meager landslide constrained by its force history derived from seismic data. *Journal of Geophysical Research: Solid Earth*, *120*, 2579–2599. https://doi.org/10.1002/2014JB011426
Moretti, L., Mangeney, A., Capdeville, Y., Stutzmann, E., Huggel, C., Schneider, D., & Bouchut, F. (2012). Numerical modeling of the Mount Steller landslide flow history and of the generated long period seismic waves. *Geophysical Research Letters*, *39*, L16402. https://doi.org/10.1029/2012GL052511
Munson, B. R., Rothmayer, A. P., Okiishi, T. H., & Huebsch, W. W. (2012). *Fundamentals of Fluid Mechanics* (7th ed., 580pp.). John Wiley & Sons.
Murray, T., Nettles, M., & Selmes, N. (2015). Reverse glacier motion during iceberg calving and the cause of glacial earthquakes. *Science*, *349*(6245), 305–308.
Murray, T., Selmes, N., James, T. D., Edwards, S., Martin, I., O'Farrell, T., et al. (2015). Dynamics of glacier calving at the ungrounded margin of Helheim Glacier, southeast Greenland. *Journal of Geophysical Research: Earth Surface*, *120*, 964–982. https://doi.org/10.1002/2015JF003531
Nettles, M., & Ekström, G. (2010). Glacial earthquakes in Greenland and Antarctica. *Annual Review of Earth and Planetary Sciences*, *38*, 467–491.
O'Neel, S., Marshall, H., McNamara, D., & Pfeffer, W. (2007). Seismic detection and analysis of icequakes at Columbia Glacier, Alaska. *Journal of Geophysical Research*, *112*, F03S23. https://doi.org/10.1029/2006JF000595
Oksanen, P., & Keinonen, J. (1982). The mechanism of friction of ice. *Wear*, *78*(3), 315–324.
Olsen, K. G., & Nettles, M. (2017). Patterns in glacial-earthquake activity around Greenland, 2011–13. *Journal of Glaciology*, *63*(242), 1077–1089.
Petrenko, V., & Whitworth, R. (1999). Physics of ice (pp. 373).
Podolskiy, E. A., & Walter, F. (2016). *Cryoseismology, Reviews of geophysics*, *54*(4), 708–758.
Rosenau, R., Schwalbe, E., Maas, H.-G., Baessler, M., & Dietrich, R. (2013). Grounding line migration and high-resolution calving dynamics of Jakobshavn Isbræ, west Greenland. *Journal of Geophysical Research: Earth Surface*, *118*, 382–395. https://doi.org/10.1029/2012JF002515
Schulson, E. M., & Fortt, A. L. (2012). Friction of ice on ice. *Journal of Geophysical Research*, *117*, B12204. https://doi.org/10.1029/2012JB009219
Sergeant, A., Mangeney, A., Stutzmann, E., Montagner, J.-P., Walter, F., Moretti, L., & Castelnau, O. (2016). Complex force history of a calving-generated glacial earthquake derived from broadband seismic inversion. *Geophysical Research Letters*, *43*, 1055–1065. https://doi.org/10.1002/2015GL066785
Smith, S. D., & Banke, E. G. (1983). The influence of winds, currents and towing forces on the drift of icebergs. *Cold Regions Science and Technology*, *6*(3), 241–255.
Tsai, V. C., & Ekström, G. (2007). Analysis of glacial earthquakes. *Journal of Geophysical Research*, *112*, F03S22. https://doi.org/10.1029/2006JF000596
Tsai, V. C., Rice, J. R., & Fahnestock, M. (2008). Possible mechanisms for glacial earthquakes. *Journal of Geophysical Research*, *113*, F03014. https://doi.org/10.1029/2007JF000944
Vaughan, D. G. (1995). Tidal flexure at ice shelf margins. *Journal of Geophysical Research*, *100*(B4), 6213–6224.
Veitch, S. A., & Nettles, M. (2012). Spatial and temporal variations in Greenland glacial-earthquake activity, 1993–2010. *Journal of Geophysical Research*, *117*, F002412. https://doi.org/10.1029/2012JF002412
Wagner, T. J., James, T. D., Murray, T., & Vella, D. (2016). On the role of buoyant flexure in glacier calving. *Geophysical Research Letters*, *43*, 232–240. https://doi.org/10.1002/2015GL067247
Walter, F., Amundson, J. M., O'Neel, S., Truffer, M., Fahnestock, M., & Fricker, H. A. (2012). Analysis of low-frequency seismic signals generated during a multiple-iceberg calving event at jakobshavn isbræ, Greenland. *Journal of Geophysical Research*, *117*, F01036. https://doi.org/10.1029/2011JF002132
Walter, F., O'Neel, S., McNamara, D., Pfeffer, W., Bassis, J. N., & Fricker, H. A. (2010). Iceberg calving during transition from grounded to floating ice: Columbia glacier, alaska. *Geophysical Research Letters*, *37*, L15501. https://doi.org/10.1029/2010GL043201
Walter, F., Olivieri, M., & Clinton, J. F. (2013). Calving event detection by observation of seiche effects on the Greenland fjords. *Journal of Glaciology*, *59*(213), 162–178.
Wendel, K. (1956). Hydrodynamic masses and hydrodynamic moments of inertia, Ph.D. thesis. Hamburg, translated to English by E.N. Labouvie and Avis Borden. Washington, DC: Navy Department. Retrieved from https://dome.mit.edu/handle/1721.3/51294
Xie, S., Dixon, T. H., Voytenko, D., Holland, D. M., Holland, D., & Zheng, T. (2016). Precursor motion to iceberg calving at Jakobshavn Isbræ, Greenland, observed with terrestrial radar interferometry. *Journal of Glaciology*, *62*(236), 1134–1142.
Yamada, M., Mangeney, A., Matsushi, Y., & Matsuzawai, T. (2018). Estimation of dynamic friction and movement history of large landslides, Landslides, F1, https://doi.org/10.1007/s10346-018-1002-4
Yamada, M., Mangeney, A., Matsushi, Y., & Moretti, L. (2018). Estimation of dynamic friction process of the Akatani landslide based on the waveform inversion and numerical simulation. *Geophysical Journal International*, *206*, 1479–1486.
Yvin, C., Leroyer, A., Visonneau, M., & Queutey, P. (2018). Added mass evaluation with a finite-volume solver for applications in fluid–structure interaction problems solved with co-simulation. *Journal of Fluids and Structures*, *81*, 528–546.
Zhao, J., Moretti, L., Mangeney, A., Stutzmann, E., Kanamori, H., Capdeville, Y., et al. (2014). Model space exploration for determining landslide source history from long-period seismic data. *Pure and Applied Geophysics*, *172*, 389–413. https://doi.org/10.1007/s00024-014-0852-5

Supporting Information for "Numerical modeling of iceberg capsize responsible for glacial earthquakes"

Amandine Sergeant[1,2,3], Vladislav A. Yastrebov[4], Anne Mangeney[1,2,5],

Olivier Castelnau[6], Jean-Paul Montagner[1,2], Eléonore Stutzmann[1]

Corresponding author: Amandine Sergeant, Versuchsanstalt für Wasserbau, Hydrologie und Glaziologie, ETH Zürich, Hönggerbergring 26, 8093 Zürich, Switzerland. (sergeant@vaw.baug.ethz.ch)

[1]Institut de Physique du Globe de Paris,

CNRS UMR 7154, Université Paris

Diderot-Paris 7, Paris, France

[2]Université Paris Diderot, Paris, France

[3]Now at Versuchsanstalt für Wasserbau,

Hydrologie und Glaziologie (VAW), ETH

Zürich, CH-8092 Zürich, Switzerland

(sergeant@vaw.baug.ethz.ch)

[4]MINES ParisTech, PSL Research

University, Centre des Matériaux, CNRS

UMR 7633, Evry, France

[5]ANGE team, INRIA, Laboratoire

Jacques-Louis Lions, Paris, France

[6]Processes and Engineering in Mechanics
and Materials, CNRS UMR 8006, ENSAM,
CNAM, Paris, France

Contents of this file

1. Text S1: Discussion related to figure S2 and influence of initial buoyant conditions on the capsize force.

2. Figure S1: Drag effect on force magnitudes with the iceberg aspect ratio.

3. Figure S2: Effects of non-buyant initial conditions on the force spectral amplitudes at specific frequencies.

4. Movie S1: Animation of the bottom-out capsize of an iceberg of aspect ratio $\epsilon = 0.2$ and height $H = 800$ m, and associated contact force $F_c(t)$.

5. Movie S2: Animation of the topout capsize of an iceberg of aspect ratio $\epsilon = 0.2$ and height $H = 800$ m, and associated contact force $F_c(t)$.

6. Movie S3: Animation of the bottom-out capsize of a subaerial iceberg of aspect ratio $\epsilon = 0.1$ and height $H = 800$ m, and associated contact force $F_c(t)$.

Text S1.

As shown in the main body of the paper, initial buoyant conditions of the iceberg impacts the contact force. When they capsize, subaerial icebergs ($\Delta < 0$) generate a force whose spectral amplitudes are amplified at specific frequencies, noted f_{plus}. Similarly, submarine icebergs ($\Delta > 0$) generate a force with strong energy gap at frequencies f_{gap}. Figure S2 shows the evolution of these frequencies with the aspect ratio ϵ of the iceberg. The results presented here are for BO icebergs with $H = 800$ m. The same tendencies are observed for other iceberg heights but with slight shifts of f_{plus} and f_{gap} values toward higher or lower frequencies. For 600 m-height icebergs, they vary within the range 0.018-0.3 Hz. For 1000 m-height icebergs, they vary between 0.012 and 0.02 Hz. We also evaluate associated perturbations ΔA of the force spectral amplitudes at corresponding frequencies $f_0 = f_{\text{plus}}$ or $f_0 = f_{\text{gap}}$, with respect to the spectral amplitude of the neutral force as:

$$\Delta A(f_0) = \frac{A_{\Delta z}(f_0) - A_{z_w}(f_0)}{A_{z_w}(f_0)} \tag{1}$$

A represents the spectral amplitude, $A_{\Delta z}$ is for Δz-pertubated icebergs, A_{z_w} is for neutrally buoyant icebergs. Positive $\Delta A(f_{\text{plus}})$ are associated with subaerial icebergs. Negative $\Delta A(f_{\text{gap}})$ associated with submarine icebergs.

Figure S1. (a) Force magnitudes A (kg.m) computed by integrating the contact force twice with respect to time, for no drag (filled circles) and drag (open circles). The results are for bottom-out icebergs of unit length L. (b) Evolution of the ratio of the force magnitudes (drag/no drag) with ϵ. This shows that pressure drag greatly changes the capsize dynamics especially for thin icebergs.

Figure S2. Variation of the frequency (b) f_{plus} for the secondary force spectral peaks associated with subaerial icebergs, and (c) f_{gap} for the force energy gaps associated with submarine icebergs, with ϵ. Variation of the perturbations of force spectral amplitudes ΔA induced by $\Delta z \neq 0$ and measured at frequencies (d) f_{plus} and (e) f_{gap}, with aspect ratio. Results are for bottom-out icebergs with $H = 800$ m.

Movie S1. Animation of the bottom-out capsize of an iceberg of aspect ratio $\epsilon = 0.2$ and height $H = 800$ m, and associated force $F_c(t)$. The iceberg is initially at its hydrostatic equilibrium. The color scale represents horizontal stress σ_{xx}. Gray shaded area represents water.

Movie S2. Animation of the top-out capsize of an iceberg of aspect ratio $\epsilon = 0.2$ and height $H = 800$ m, and associated force F_c. The iceberg is initially at its hydrostatic equilibrium. The color scale represents horizontal stress σ_{xx}. Gray shaded area represents water.

Movie S3. Animation of the bottom-out capsize of a subaerial iceberg of aspect ratio $\epsilon = 0.1$ and height $H = 800$ m which experiences a water level $z_0 = z_w - 10$ m. Associated contact force F_c is plotted on the bottom panel. The color scale represents horizontal stress σ_{xx} of solid bodies. Gray shaded area represents water.

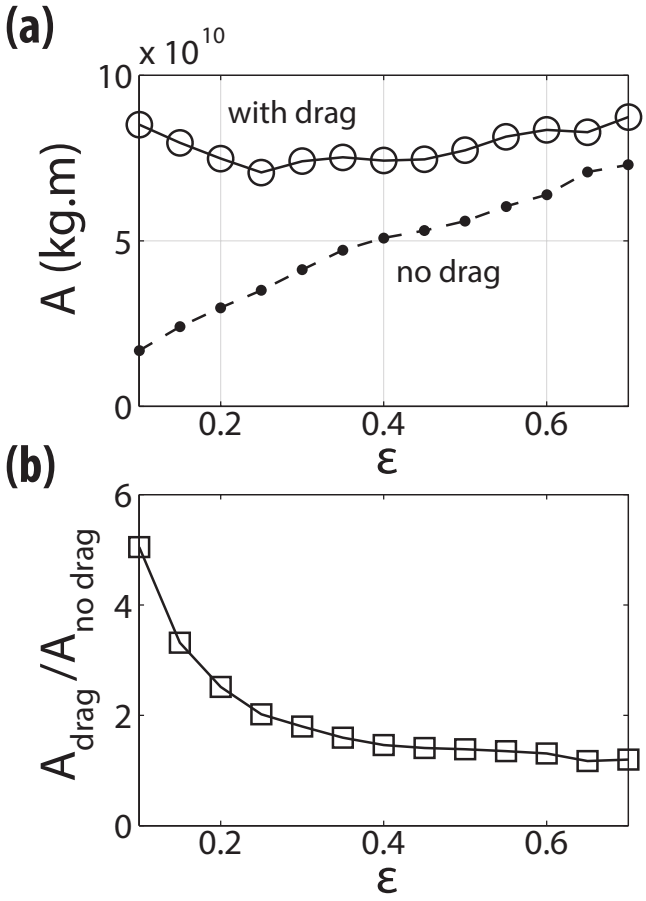

Figure S1. (a) Force magnitudes A (kg.m) computed by integrating the contact force twice with respect to time, for no drag (filled circles) and drag (open circles). The results are for bottom-out icebergs of unit length L. (b) Evolution of the ratio of the force magnitudes (drag/no drag) with ϵ. This shows that pressure drag greatly changes the capsize dynamics especially for thin icebergs.

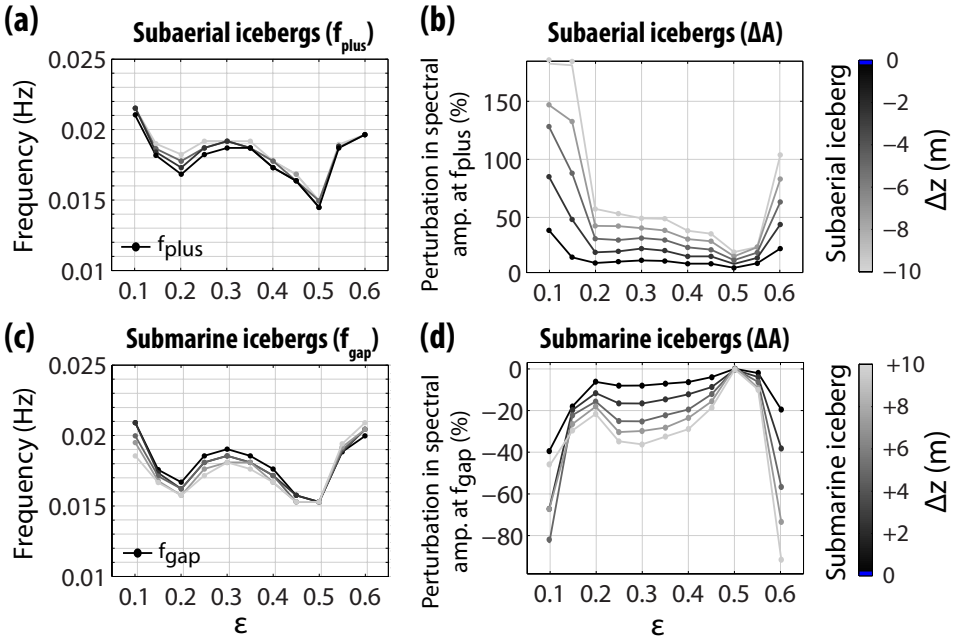

Figure S2. Variation of the frequency (b) $f_{\rm plus}$ for the secondary force spectral peaks associated with subaerial icebergs, and (c) $f_{\rm gap}$ for the force energy gaps associated with submarine icebergs, with ϵ. Variation of the perturbations of force spectral amplitudes ΔA induced by $\Delta z \neq 0$ and measured at frequencies (d) $f_{\rm plus}$ and (e) $f_{\rm gap}$, with aspect ratio. Results are for bottom-out icebergs with $H = 800$ m.

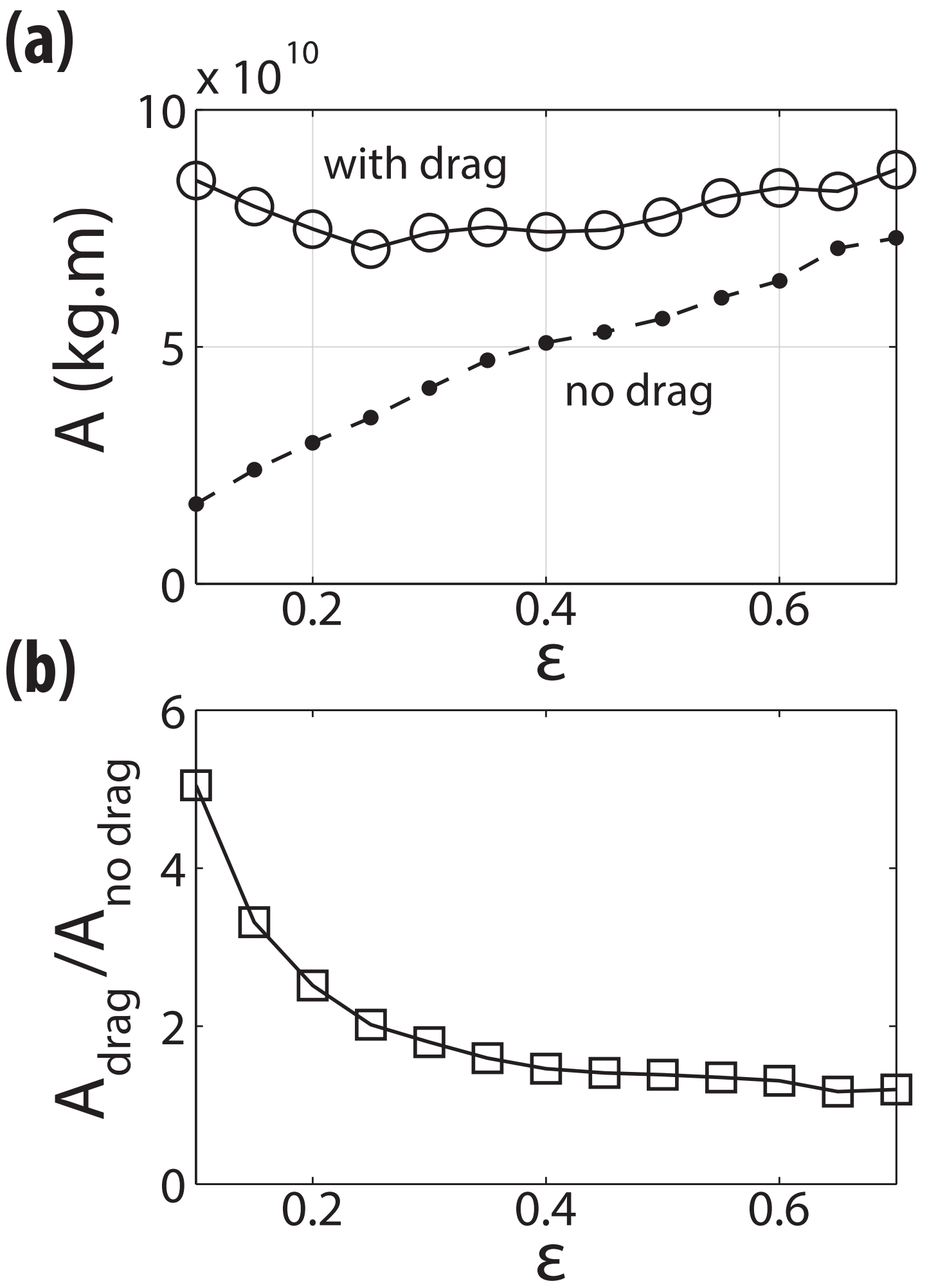
(a)
x 10^10
10
5
0
A (kg.m)
with drag
no drag
0.2
0.4
0.6
ε
(b)
6
4
2
0
A_drag /A_no drag
0.2
0.4
0.6
ε

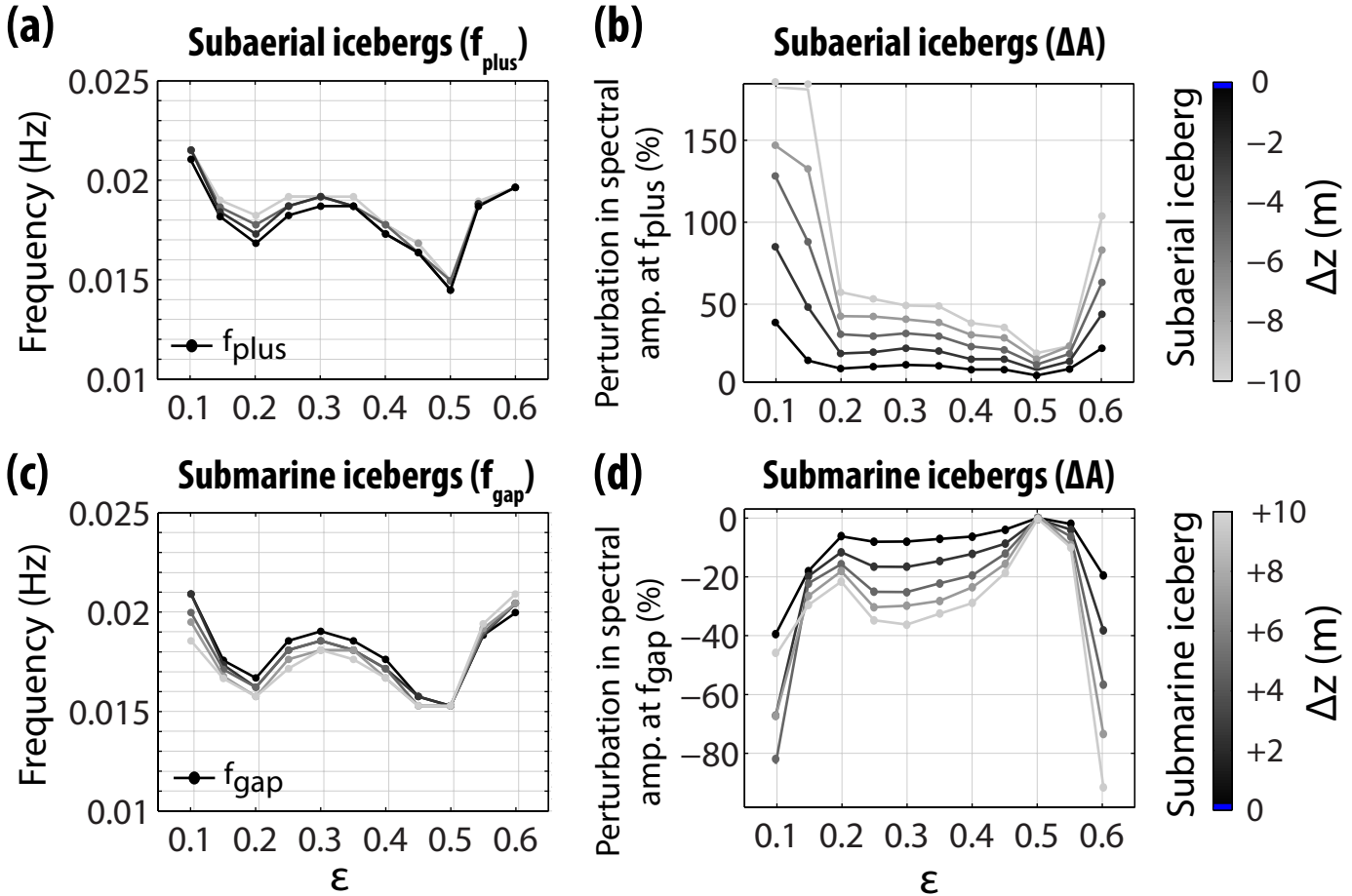
(a)
Subaerial icebergs (f plus)
Frequency (Hz)
0.025
0.02
0.015
0.01
f plus
0.1 0.2 0.3 0.4 0.5 0.6
(b)
Subaerial icebergs (ΔA)
Perturbation in spectral amp. at f plus (%)
150
100
50
0
Subaerial iceberg
0
−2
−4
−6
−8
−10
Δz (m)
(c)
Submarine icebergs (f gap)
Frequency (Hz)
f gap
ε
(d)
Submarine icebergs (ΔA)
Perturbation in spectral amp. at f gap (%)
−20
−40
−60
−80
Submarine iceberg
+10
+8
+6
+4
+2
Δz (m)